



Superomniphobic Surfaces for Military Applications: Nano- and Micro-Fabrication Methods

Chapter 1: Lithographic Fabrication of Surfaces with Different Microgeometries and Investigation of Their Wetting Behaviour

Alidad Amirkazli
University of Alberta

*University of Alberta
Department of Mechanical Engineering
Edmonton, AB T6G 2G8*

*PWGSC Contract Number: W7707-098197
Contract Scientific Authority: Paul Saville, 250-363-2892*

The scientific or technical validity of this Contract Report is entirely the responsibility of the contractor and the contents do not necessarily have the approval or endorsement of Defence R&D Canada.

Defence R&D Canada – Atlantic

Contract Report
DRDC Atlantic CR 2010-329
January 2011

Canada

This page intentionally left blank.

Superomniphobic Surfaces for Military Applications: Nano- and Micro-Fabrication Methods

Chapter 1: Lithographic Fabrication of Surfaces with Different Microgeometries and Investigation of Their Wetting Behaviour

Alidad Amirfazli
University of Alberta

University of Alberta
Department of Mechanical Engineering
Edmonton, Alberta T6G 2G8

PWGSC Contract Number: W7707-098197
CSA: Paul Saville, 250-363-2892

The scientific or technical validity of this Contract Report is entirely the responsibility of the Contractor and the contents do not necessarily have the approval or endorsement of Defence R&D Canada.

Defence R&D Canada – Atlantic

Contract Report
DRDC Atlantic CR 2010-329
January 2011

Principal Author

Original signed by Alidad Amirfazli

Alidad Amirfazli

Approved by

Original signed by Terry Foster

Terry Foster

Head Dockyard Laboratory Pacific

Approved for release by

Original signed by Ron Kuwahara for

Calvin Hyatt

Head Document Review Panel

This Work Sponsored by 12S through 12SZ20

- © Her Majesty the Queen in Right of Canada, as represented by the Minister of National Defence, 2011
- © Sa Majesté la Reine (en droit du Canada), telle que représentée par le ministre de la Défense nationale, 2011

Abstract

Recent rapid improvements of micro/nanofabrication techniques have allowed us to prepare patterned surfaces with controlled topographic structures. In this report, three kinds of patterned surfaces, i.e., square, triangle and circle post array surfaces, have been prepared on silicon wafers. On such surfaces, for the same roughness or solid-liquid contact fraction value, different surface textures can exhibit completely different wetting behaviour. Effects of various microgeometrical parameters, such as length scale effect, edge/corner pinning effect, geometrical shape effect, direction-dependent effect, etc., on wetting have been investigated. For the patterned surfaces with fixed solid area fraction, a smaller microgeometrical length scale can induce a smaller advancing contact angle and a larger receding contact angle, when it is compared to a larger microgeometrical length scale. Competing factors such as solid area fraction and solid linear fraction are found to be responsible for such effects. Moreover, it is also revealed that there is a strong dependence of directions for surface wettability on the patterned surfaces. Different edge/corner pinning effects, including the pinning length and pinning point density, in various directions are suggested to be taken into consideration for affecting the surface wetting behaviour.

Résumé

Les progrès rapides qu'ont connus récemment les techniques de microfabrication et de nanofabrication nous ont permis de préparer des surfaces à motif qui possèdent des structures topographiques contrôlées. Dans le cadre des travaux qui font l'objet du présent rapport, trois types de surfaces à motif ont été préparées sur des plaquettes de silicium, soit des surfaces post-matrice à carrés, à triangles et à cercles. Pour des surfaces de cette nature qui présentent une rugosité identique et une valeur égale de la fraction de contact solide-liquide, les diverses textures superficielles des surfaces peuvent avoir un comportement au mouillage totalement différent. On a étudié les effets de divers paramètres microgéométriques sur le mouillage, notamment l'effet d'échelle de longueur, l'effet d'ancrage des bords et des coins, l'effet de la forme géométrique et l'effet qui dépend de l'orientation. Dans le cas des surfaces à motif qui présentent une fraction superficielle solide fixe, une faible échelle de longueur microgéométrique peut se traduire par un angle de contact à l'avancement plus petit et un angle de contact au retrait plus important, comparativement à une échelle plus large. Les résultats indiquent qu'un effet de cette nature est attribuable à des facteurs concurrentiels tels que la fraction superficielle solide et la fraction linéaire solide. De plus, ils révèlent que la mouillabilité superficielle des surfaces à motif dépend grandement des orientations des caractéristiques. Les données laissent supposer qu'il faut tenir compte de différents effets d'ancrage des bords et des coins, y compris la longueur d'ancrage et la densité des points d'ancrage, dans le cas de diverses orientations, car ils pourraient influer le comportement au mouillage de la surface.

This page intentionally left blank.

Executive summary

Superomniphobic Surfaces for Military Applications: Nano- and Micro-Fabrication Methods: Chapter 1: Lithographic Fabrication of Surfaces with Different Microgeometries and Investigation of Their Wetting Behaviour

Alidad Amirfazli; DRDC Atlantic CR 2010-329; Defence R&D Canada – Atlantic; January 2011

Introduction: The production of materials that are not wetted depends on having the surfaces having low surface energy and roughness that reduce the contact area and adhesion between the liquid and solid. Although materials can be made which possess these qualities their wetting behaviour is not always consistent with liquids becoming pinned on the surface or experiencing different advancing and receding contact angles. In this study lithography is used to produce structured surfaces which are highly controlled. Basic arrays of cylindrical, triangular and square columns were fabricated in order to gain insight on the various microgeometrical factors that affect the wetting of a surface.

Results: For the patterned surfaces with fixed solid area fraction, a smaller microgeometrical length scale can induce a smaller advancing contact angle and a larger receding contact angle, when it is compared to a larger microgeometrical length scale. Competing factors such as solid area fraction and solid linear fraction are found to be responsible for such effects. Moreover, it is also revealed that there is a strong dependence on direction for surface wettability on the patterned surfaces. Different edge/corner pinning effects, including the pinning length and pinning point density, in various directions are suggested to be taken into consideration for affecting the surface wetting behaviour.

Significance: If microtextured lithographically produced surfaces are to be used to produce superhydrophobic/ superomniphobic properties by a rapid production method such as hot embossing, then it is important to know the factors that control the wetting behaviour so that materials with controlled properties can be prepared. Such materials may prove to be beneficial in the reduction of contamination of personnel and equipment by chemical agents, toxic industrial chemicals and they may provide other benefits such as better antenna performance and improved optical clarity in inclement weather

Future plans: This work is part of a TIF project investigating super organophobic materials. The work on microgeometrical factors will be extended by considering adhesive forces as a function of the geometrical factors including edge pinning. Wear performance of superhydrophobic materials is being considered as well.

Sommaire

Superomniphobic Surfaces for Military Applications: Nano- and Micro-Fabrication Methods: Chapter 1: Lithographic Fabrication of Surfaces with Different Microgeometries and Investigation of Their Wetting Behaviour

Alidad Amirfazli; DRDC Atlantic CR 2010-329; R & D pour la défense Canada – Atlantique; Janvier 2011

Introduction : La production de matériaux non mouillés dépend de certains facteurs, par exemple le fait que leurs surfaces doivent présenter une faible énergie superficielle et une rugosité peu importante, ce qui réduit l'aire contact et l'adhérence entre le liquide et le solide. Il est possible de fabriquer des matériaux qui possèdent ces propriétés, mais leur comportement au mouillage n'est pas toujours compatible avec le processus d'ancrage du liquide à la surface ou la variation des angles de contact à l'avancement et au retrait. Dans le cadre de l'étude faisant l'objet du présent rapport, on a utilisé la lithographie pour produire des surfaces structurées ayant des propriétés étroitement contrôlées. Des matrices de base de colonnes cylindriques, triangulaires et carrées ont été fabriquées afin d'éclaircir la nature des différents facteurs microgéométriques qui influent sur le mouillage de la surface.

Résultats : Dans le cas des surfaces à profil ayant une fraction superficielle solide fixe, une faible échelle de longueur microgéométrique peut se traduire par un angle de contact à l'avancement plus petit et un angle de contact au retrait plus important, comparativement à une échelle plus large. Les résultats indiquent qu'un effet de cette nature est attribuable à des facteurs concurrentiels tels que la fraction superficielle solide et la fraction linéaire solide. De plus, ils révèlent que la mouillabilité superficielle des surfaces à motif dépend grandement des orientations des caractéristiques. Les données laissent supposer qu'il faut tenir compte de différents effets d'ancrage des bords et des coins, y compris la longueur d'ancrage et la densité des points d'ancrage, dans le cas de diverses orientations, car ils pourraient influer le comportement au mouillage de la surface.

Importance : Si on prévoit utiliser des surfaces dont la microtexture est produite par lithographie pour obtenir des propriétés superhydrophobes ou superomniphobes au moyen d'une méthode de production rapide comme celle de gaufrage à chaud, il est important de déterminer clairement les facteurs qui influent sur le comportement au mouillage, et ce, afin de préparer des matériaux possédant des propriétés bien contrôlées. Des matériaux de ce type pourraient présenter des avantages au chapitre de la réduction de la contamination du personnel et de l'équipement par des agents chimiques ou des produits chimiques industriels toxiques; de plus, ils pourraient aussi permettre d'améliorer la performance des antennes et la clarté optique de dispositifs soumis à des conditions climatiques rigoureuses.

Perspectives : Les travaux faisant l'objet du présent rapport sont exécutés dans le cadre d'un projet du FIT qui porte sur l'étude de matériaux superorganophobes. La portée des travaux sur les facteurs microgéométriques sera étendue, notamment en tenant compte du comportement des

forces d'adhérence en fonction de certains facteurs géométriques, dont l'ancrage des bords. On envisage aussi d'étudier la performance à l'usure des matériaux superhydrophobes.

This page intentionally left blank.

Table of contents

Abstract	i
Résumé	i
Executive summary	iii
Sommaire	iv
Table of contents	vii
List of figures	viii
List of tables	x
1 Overview.....	1
2 Introduction.....	2
2.1 Theoretical Basis	3
2.1.1 Equilibrium CAs	3
2.1.2 Advancing and Receding CAs for Composite State	4
3 Experimental Methods.....	10
3.1 Experimental Design	10
3.2 Preparation of Patterned Silicon Substrates.....	12
3.3 Surface Modification	14
3.4 Surface Characterization	14
3.5 Contact Angle Measurements.....	14
4 Results and Discussion	15
4.1 Wetting on Hydrophilic Patterned Surfaces	17
4.2 Wetting on Hydrophobic Patterned Surfaces	19
4.2.1 CAs from Azimuthal Angle of Zero Degree.....	19
4.2.1.1 Receding CA Analysis.....	21
4.2.1.2 Advancing CA Analysis	22
4.2.1.3 CAs from other Azimuthal Angles	25
5 Conclusions.....	29
6 Future Works	30
References	31
Annex A .. Supplemental Information for Chapter 1	35
List of symbols/abbreviations/acronyms/initialisms	41
Distribution list	43

List of figures

Figure 1. Schematic top views of drop DCL for the drop on a patterned surface with square post array (not to scale). (a) The inset shows the DCL shape on a large length scale microgeometrical surface. (b) DCL shape on a small length scale microgeometrical surface. Note that the dashed cells refer to the repetitive units..... 7

Figure 2. An enlarged side view near the receding contact line of a drop suspended on the posts: 1-2 the drop contact line is retreating on the flat post top with a local receding CA equal to that exhibited on the smooth surface (θ_{r0}); 3-4 the contact line is pinned on the edge; 5 a new contact point is formed on the nearest post after depinning happens at 4; 6 theoretical contact line movement with local receding CA (θ_{r0}) on the side of the post, which will unlikely happen on a hydrophobic post with the solid edge angle $\Phi=90^\circ$ 8

Figure 3. An enlarged side view near the advancing contact line of a drop suspended on the posts: 1-2 the drop contact line is propagating on the flat post top with an advancing CA equal to that exhibited on the smooth surface (θ_{a0}); 3-4 the contact line is pinned on the corner; 5 a new contact point is formed on the nearest post when the meniscus of 4 is oscillating around its equilibrium position; 6 theoretical contact line movement with advancing CA (θ_{a0}) on the side of the post, which will unlikely happen on a hydrophobic post with solid edge angle $\Phi=90^\circ$ 9

Figure 4. Schematic depiction of top views for patterned surfaces with different microgeometries. The dashed cells refer to the repetitive units. Images of drops sitting on the post arrays were taken from azimuthal angle of (a) 0° , (b) 45° and (c) 90° relative to x axis. 10

Figure 5. A schematic illustration for the micromachining procedure on silicon wafers. The thermal oxidation process is to ensure chemical homogeneity. 13

Figure 6. (a) A patterned silicon substrate by lithography and RIE techniques with drilled holes on. (b) A patterned silicon substrate mounted on the stage of a contact angle measuring system with syringe below to create a drop on top of the surface. 13

Figure 7. Images of water drops sitting on (a) smooth SWT surface; (b) smooth SWT surface treated by C_4F_8 passivation..... 15

Figure 8. SEM images of the surfaces patterned with (a) Square posts, (b) Triangle posts and (c) circle posts for microstructures of Table 1, post height 30 μm . The insets show the top views of the microstructures with different post shapes. 16

Figure 9. (a) Side and (b) top views for water drop on the square post array (Table 1, post height=20 μm) before surface modification. Note that the syringe is underneath the drop through the hole. The insets show the time sequence. 18

Figure 10. (a) Water drop sitting on the patterned surface. (b) A partial enlargement at the three phase contact point which is artificially magnified by three times. Note that light can penetrate through the post spacing (square post array of Table 3 with height 30 μm). 19

Figure 11. Variations of advancing (θ_a) and receding (θ_r) contact angles with respect to pattern types and geometrical parameters corresponding to Tables 1 (T1: $f_a = 0.28$, $S = 256\mu\text{m}^2$), 2 (T2: $f_a = 0.28$, $S = 64\mu\text{m}^2$) and 3 (T3: $f_a = 0.071$, $S = 64\mu\text{m}^2$) (a) for post height 20 μm and (b) post height 30 μm . Note that the CAs were measured from azimuthal angle of 0 degree.	20
Figure 12. The comparison between the experimental apparent receding CA data and theoretically predicted apparent receding CAs for square post arrays. Note that the experimental data noted by symbol * is from Dorrer's experiment. ³⁹	22
Figure 13. Variations of CAH with respect to pattern types and geometrical parameters corresponding to Tables 1 (T1: $f_a = 0.28$, $S = 256\mu\text{m}^2$), 2 (T2: $f_a = 0.28$, $S = 64\mu\text{m}^2$) and 3 (T3: $f_a = 0.071$, $S = 64\mu\text{m}^2$) (a) for post height 20 μm and (b) post height 30 μm . Note that the CAs were measured from azimuthal angle of 0 degree.....	24
Figure 14. Schematic top views of two square post columns from azimuthal angles (not to scale) (a) 0 degree and (b) 45 degree. Note that the shapes of contact line are shown when the DCLs reach the post edges.	26
Figure 15. Schematic top views of two circle post columns from azimuthal angles (not to scale) (a) 0 degree and (b) 45 degree. Note that the shapes of contact line are shown when the drop DCLs reach the post edges.....	27
Figure 16. Schematic top view of triangle post array from azimuthal angle of 90 degree. L1, L2 and L3 represent the DCL at the right side of the drop; L4, L5 and L6 represent DCL at the left side of the drop.	28

List of tables

Table 1. The project goals for year one.....	1
Table 2. Theoretical settings for microgeometries ($f_a = 0.28$, $S=256\mu\text{m}^2$). a, b and h represent the post width, spacing and height, respectively; f_a , r_w represent the solid area fraction and Wenzel's roughness, respectively; θ_C and θ_w represent the CAs from Cassie's and Wenzel's equations, respectively; P and S represent the edge length density and length scale, respectively; θ_Y is 111° which is assumed to be the average of advancing and receding CAs on smooth surface.....	11
Table 3. Theoretical settings for microgeometries with smaller length scale ($f_a = 0.28$, $S=64\mu\text{m}^2$)	11
Table 4. Theoretical settings for microgeometries smaller f_a ($f_a=0.071$, $S=64\mu\text{m}^2$).....	12
Table 5. CA measurement on smooth silicon wafers. Silicon wafers untreated (SWU); silicon wafers treated (SWT) in 900°C (10min), SiO_2 thickness: 70nm; SWU + C_4F_8 passivation (90sec.), polymer thickness: 60nm; SWT + C_4F_8 passivation (90sec.), polymer thickness: 60nm. Note that SD is the standard deviation for measurements.....	15
Table 6. CA Measurement on Patterned Surfaces from Various Azimuthal angles (For Microgeometries of Table 1, Post height= $20\mu\text{m}$); note that SD is the standard deviation for measurements.	26
Table A1-7. L-Edit settings and experimental results for square post arrays of microgeometrical parameters corresponding to Table 1 ($S=256$, $f_a=0.28$).....	35
Table A1-8. L-Edit settings and experimental results for triangle post arrays of microgeometrical parameters corresponding to Table 1 ($S=256$, $f_a=0.28$).....	35
Table A1-9. L-Edit settings and experimental results for circle post arrays of microgeometrical parameters corresponding to Table 1 ($S=256$, $f_a=0.28$).....	36
Table A1-10. L-Edit settings and experimental results for square post arrays of microgeometrical parameters corresponding to Table 2 ($S=64$, $f_a=0.28$).....	36
Table A1-11. L-Edit settings and experimental results for triangle post arrays of microgeometrical parameters corresponding to Table 2 ($S=64$, $f_a=0.28$).....	36
Table A1-12. L-Edit settings and experimental results for circle post arrays of microgeometrical parameters corresponding to Table 2 ($S=64$, $f_a=0.28$).....	37
Table A1-13. L-Edit settings and experimental results for square post arrays of microgeometrical parameters corresponding to Table 3 ($S=64$, $f_a=0.071$)	37
Table A1-14. L-Edit settings and experimental results for triangle post arrays of microgeometrical parameters corresponding to Table 3 ($S=64$, $f_a=0.071$)	37
Table A1-15. L-Edit settings and experimental results for circle post arrays of microgeometrical parameters corresponding to Table 3 ($S=64$, $f_a=0.071$)	38

Table A2-16. Variations of advancing (θ_a), receding (θ_r) CAs and contact angle hysteresis (CAH) with respect to pattern types and geometrical parameters corresponding to Tables 1 (T1: $f_a = 0.28$, $S = 256\mu\text{m}^2$), 2 (T2: $f_a = 0.28$, $S = 64\mu\text{m}^2$) and 3 (T3: $f_a = 0.071$, $S = 64\mu\text{m}^2$) for post height 20 μm . SD represents the standard deviation for measurements.	38
Table A2-17. Variations of advancing (θ_a), receding (θ_r) CAs and contact angle hysteresis (CAH) with respect to pattern types and geometrical parameters corresponding to Tables 1 (T1: $f_a = 0.28$, $S = 256\mu\text{m}^2$), 2 (T2: $f_a = 0.28$, $S = 64\mu\text{m}^2$) and 3 (T3: $f_a = 0.071$, $S = 64\mu\text{m}^2$) for post height 30 μm . SD represents the standard deviation for measurements.	39

This page intentionally left blank.

1 Overview

This report covers the activities done regarding the TIF project in year one. The goals for the first year of the project are given in the Table 1. All these goals are met except fabrication of hierarchical surface textures. As the project progressed it became apparent the initiation of this goal would be premature, given the complexities that were described in the single scale surface texturing (see next section). Furthermore, it was recognized that development of durability criterion for superhydrophobic surfaces is a challenging task (one of the goals of year two), so it was decided to bring forward the work on this area to be able to meet the overall goal of the project on time by the end of the project period. Finally, given the applied aspects of the project for military applications, steps were taken to also produce superhydrophobic surfaces in the non-lithographic way so they would not be limited to silicon substrates and can be applied to a wider range of substrates, e.g. textile that would be of interest to the military.

Table 1. The project goals for year one.

Fabrication and characterization of basic surface textures using lithography techniques
Conducting wetting and liquid shedding experiments
Analysis of the results in connection with relation between surface texture and SH properties of the first line item of this table
Fabrication and characterization of hierarchical surface textures using lithography techniques
Conducting wetting and liquid shedding experiments

The progress made in the lithographic production of superhydrophobic surfaces are explained in Chapter 1 of this report, whereas in Chapter 2 production of superhydrophobic surfaces through nano-particle route and initial durability results are discussed in the Chapter 2 as a separate report.

2 Introduction

The wetting behaviour of surfaces, the result of the interplay between liquid and surface chemistry and roughness, is such an influential area that much research has been devoted to in the past decades.^{1,2} Understanding and controlling the wetting phenomena are significant in both fundamental research and industrial applications. As is well known, the modification of surface chemistry is one of the most effective ways to control the wetting behaviour of surfaces.^{3, 4} However, such surface chemistry modification can have some limitations, e.g., the choice of chemical species and their biochemical compatibility.⁵ The effect of surface roughness or its microgeometry on wetting has received much attention over the past.⁶⁻¹³ Particularly, the advantage of flexible manipulation of surface microgeometries allows nature to develop various special wetting properties, e.g., the self cleaning property^{14, 15} of some plant's leaves¹⁶⁻¹⁹ and animal's wings,^{20, 21} the super-floating ability of water-strider,²²⁻²⁴ the anti-fogging property of mosquito compound eyes,²⁵ the water-collection ability of spider silk²⁶ and desert beetles,²⁷⁻²⁹ etc. Moreover, with the development of micro/nanofabrication technologies, various surface microgeometries preparations have been proposed to control the surface wettability.^{30, 31}

The apparent contact angle (CA, the angle at which a liquid/vapor interface meets a solid surface) on rough surfaces correlated with roughness (r) or solid-liquid contact area fraction (f_a) was well formulated more than 60 years ago,^{32, 33} i.e., the classical Wenzel and Cassie equations. It has been widely used to characterize the surface drop repellency,³⁴ especially for superhydrophobic surfaces (SHS) studied in recent years.^{14, 15} However, these equations maybe inadequate to comprehend another important SHS property, i.e., the drop mobility³⁴ related to contact angle hysteresis (CAH, the difference between advancing or maximum and receding or minimum contact angles), since r or f_a represents a composite measure of all surface texture parameters and the apparent CA obtained from Wenzel or Cassie equation only represents the equilibrium or minimum-energy state.³⁵⁻³⁷ Thus it is insufficient to gain a complete understanding on the superhydrophobic wetting behaviour. On different microtextured surfaces, even for the same r and f_a values, completely different drop mobility can be observed.^{38, 39} Also, it is of interest to note that there is an intensive debate on the validity of the Wenzel and Cassie equations recently.⁴⁰⁻⁴³ Different microgeometry distributions may affect the definition of r and f_a (i.e., whether it is a global or a local value), resulting in a misuse of the Wenzel and Cassie equations to calculate the CA values. Therefore, the role of surface microgeometry in wetting behaviour cannot be fully described by r and f_a , and it is necessary to investigate the effect of other microgeometrical parameters that can affect the wetting results.

One of the most important effects of microgeometries is the sharp-edge effect,⁴⁴⁻⁵⁴ which is believed to be one of the main causes of the contact angle hysteresis. Such effect can be responsible for the pinning of the drop contact line (DCL) at an edge of a surface microstructure when DCL is moving on a rough surface. Here, the “drop contact line” (along the drop perimeter) is used instead of the “three phase contact line”, since the three phase contact line will be discontinuous and form underneath the drop for superhydrophobic wetting state where air is entrapped in the troughs of a rough surface.⁴¹ Gibbs⁵⁵ first proposed the inequality condition for a liquid DCL at a sharp solid edge based on a geometrical treatment. Following the work of Gibbs, Oliver *et al.*⁴⁴ examined Gibbs' results theoretically and experimentally, and indicated that Gibbs' edge effect is mainly a geometrical consequence immaterial to the intrinsic nature of the edge (e.g. the selective adsorption of impurities on the edge). Later, many wetting behaviours related

to pinning of DCL have been observed^{52, 53, 56-59} and explained by applying Gibbs' principle. Moreover, by employing re-entrant edge shapes, recent researches have showed that superhydrophobic behaviour can be generated from hydrophilic materials or for low surface tension liquids.⁶⁰⁻⁶⁹ Nevertheless, the pinning of DCL at the edge of surface microgeometries for SHS is still not well explained. For example, advancing and receding DCL may have a different pinning behaviour at the edge, leading to different advancing and receding CAs as well as drop mobility. Further study of the pinning of DCL at a microgeometrical edge is required.

In addition to the edge effect, the topography shape and length scale may also influence wetting behaviour particularly for superhydrophobic surfaces. Oner and McCarthy³⁸ studied the hydrophobicity of microtextured surfaces with posts of different sizes, shapes and separations. They claimed that increasing the post distance and changing the shape of the posts from square to staggered rhombus, star or indented square may decrease the contact length and increase the tortuosity of DCL and thus increase the receding contact angles. But when changing the shape of the posts, they did not keep the other surface parameters constant, e.g., the roughness or the fraction of the solid surface in contact with a drop. As a result, conclusions of the effects of the post shapes cannot be supported in the context of current theories.^{32, 33} Youngblood and McCarthy⁷⁰ and Yoshimitsu *et al.*⁷¹ have pointed out that for a drop on a microtextured surface, the drop may have a contorted DCL. They believed that serious contortion can make the contact line less continuous and unstable and thus lead to an easier drop motion. They claimed that a better design of the surface with respect to DCL shape is more effective to gain a proper surface wettability. However, no detailed design principles have been suggested. Dorrer and Ruehe^{39, 72} also discussed the influence of the distribution of the square posts on the DCL shape and then the contact angles, i.e., the advancing and receding contact angles. Though they ascribed the main reason of the effect of geometrical parameters to the shape and movement of the DCL, clear explanations still lacked.

In this report, patterned surfaces with different microgeometries, i.e., square, triangle and circle post arrays, have been fabricated by microfabrication techniques. With controlling the solid area fraction and microgeometrical length scale, various surface wetting behaviours have been investigated. Several important surface microgeometrical effects, e.g., length scale effect, edge and corner pinning effect, geometrical shape effect, direction-dependent effect, will be discussed. By applying some simplified models, mechanisms responsible for those effects can be understood.

2.1 Theoretical Basis

2.1.1 Equilibrium CAs

The thermodynamic equilibrium CA of a liquid drop on an ideal smooth solid surface can be predicted by Young's equation:

$$\gamma^{la} \cos \theta_Y = \gamma^{sa} - \gamma^{ls} \quad (1)$$

where γ_{la} , γ_{sa} and γ_{ls} are interfacial tension at liquid-air, solid-air and liquid-solid interfaces, respectively. Classically, two wetting states may occur if a drop is deposited on a rough surface: the non-composite, i.e., complete liquid penetration into the troughs of a rough surface; and the composite, i.e., entrapment of air in the troughs of a rough surface. The apparent equilibrium CA of the non-composite is given by Wenzel equation:

$$\cos \theta_w = r \cos \theta_y \quad (2)$$

where r is the roughness factor as the ratio between the actual surface area and the projected area for a wetted surface. On the other hand, the apparent equilibrium CA of the composite, θ_c , can be calculated using the Cassie equation:

$$\cos \theta_c = f_1 \cos \theta_1 + f_2 \cos \theta_2 \quad (3)$$

where f_1 and f_2 are the fractions of the solid-liquid and liquid-air interfaces with equilibrium contact angles θ_1 and θ_2 , respectively. The contact angle of liquid on solid-liquid contact part, θ_1 is equal to the Young's CA (θ_y) and liquid-air contact part, θ_2 is equal to 180° (the CA for liquid with entrapped air), as such one has:

$$\cos \theta_c = f \cos \theta_y - (1-f) \quad (4)$$

where f is the solid-liquid contact fraction of the substrate.

Recently, based on the debate of the validity of the Wenzel and Cassie equations,⁴⁰⁻⁴³ McHale⁴¹ and Nosonovsky⁴² indicated that the Cassie equation can be generalized as:

$$\cos \theta_c = f_1(x, y) \cos \theta_1 + f_2(x, y) \cos \theta_2 \quad (5)$$

The local Cassie's fractions, $f_1(x, y)$ and $f_2(x, y)$, of the two components that compose the heterogeneous surface should be taken as the functions of x and y in the region⁴² (or neighborhood⁴¹) of the DCL.

Although very high roughness factor in Eq. (2) can induce a high apparent contact angle and thus high drop repellency, low drop mobility or high contact angle hysteresis has been observed and demonstrated for Wenzel's or non-composite state. As a result, current superhydrophobic state is commonly referred to Cassie's or composite state, which will be the main subject discussed in this report.

2.1.2 Advancing and Receding CAs for Composite State

Drops on SHS may be prevented from reaching the free energy minimum states described by Eqs. (2) and (4) by multiple free energy barriers generated by the roughness.³⁶ Consequently, contact

angle hysteresis or advancing and receding CAs arises. Up to now, a quantitative prediction of advancing and receding CAs for composite state still keeps confusing.³⁷

The basis of the Cassie equation is the surface energy minimization principle. From a different perspective, nonetheless, the apparent equilibrium CA from Cassie equation Eq. (3) may also be viewed as the result of averaging the local equilibrium contact angle at the drop contact line by its length.⁴² Similarly, the apparent receding and advancing CAs can also be considered to be the result of averaging the local receding and advancing CAs along the drop contact line, which is given in a form analogous to Eq. (3) as:

$$\cos \theta_r = f_{real} \cos \theta_{s,rec} + (1 - f_{real}) \cos \theta_{air} \quad (6)$$

$$\cos \theta_a = f_{real} \cos \theta_{s,adv} + (1 - f_{real}) \cos \theta_{air} \quad (7)$$

where θ_r and θ_a is the apparent receding and advancing CAs, respectively; $\theta_{s,rec}$ and $\theta_{s,adv}$ is the local receding and advancing CAs at the solid-liquid contact part, respectively; θ_{air} is the local contact angle of the free surface between air and liquid (receding and advancing CAs equal to 180° in air); f_{real} is the real local solid-liquid contact fraction in the region of DCL. Eqs. (6) and (7) are very similar to the formulas proposed in Extrand's paper,⁷³ but $\cos \theta$ is applied rather than θ when interfacial energies is considered. In order to find the values of f_{real} , $\theta_{s,rec}$ and $\theta_{s,adv}$, we take the regularly patterned surface with square post array for example. Schematic top views of DCL for a drop resting on the patterned surface are illustrated in Figure 1. The post width and spacing are noted to be a and b , respectively.

For the real local solid-liquid contact fraction f_{real} in the region of DCL, there are two statements. The most common expression of the local contact fraction is considered as a local solid-liquid contact area fraction (we call it solid area fraction f_a) of the contact line.^{41, 43} Note that for a uniformly patterned surface, the global solid area fraction is equal to the local solid area fraction in the region of DCL. Taking the square post array for example, the solid-liquid area fraction equals to:

$$f_a = a^2 / (a^2 + b^2 + 2ab) \quad (8)$$

where a and b are corresponding to the parameters shown in Figure 1. On the other hand, as discussed by Extrand,^{73, 74} the local contact fraction is treated as a local linear fraction of the contact line (we call it solid linear fraction f_l), which equals to:

$$f_l = a / (a + b) \quad (9)$$

However, f_a is valid only when the length scale of a and b should be comparable to the thickness of the liquid-air interface (on the order of molecular dimensions, 10^{-9} ~ 10^{-8} m)⁴² and thus DCL can cover the total area of a repetitive cell unit, see Figure 1a; f_l is valid only when the contact line of the drop is assumed to be straight and local curvatures of the contact line can be ignored (in fact, the contact line between posts is really not a line but is liquid-air interface⁷² which can cover the

repetitive cell unit partly). As a result, for the length scale in micrometer (the length scale discussed in this report), the real local solid-liquid contact fraction f_{real} can be underestimated if the solid area fraction f_a is used; on the contrary, the real solid-liquid contact fraction f_{real} can also be overestimated if the solid linear fraction f_l is used. As experimentally demonstrated in Section 4, f_{real} shows a value between f_a and f_l ; by decreasing the length scale, f_{real} will decrease and finally approach to f_a , attributing to the reason that the repetitive cell unit may be closer to the DCL for small length scale microstructures, see Figure 1b.

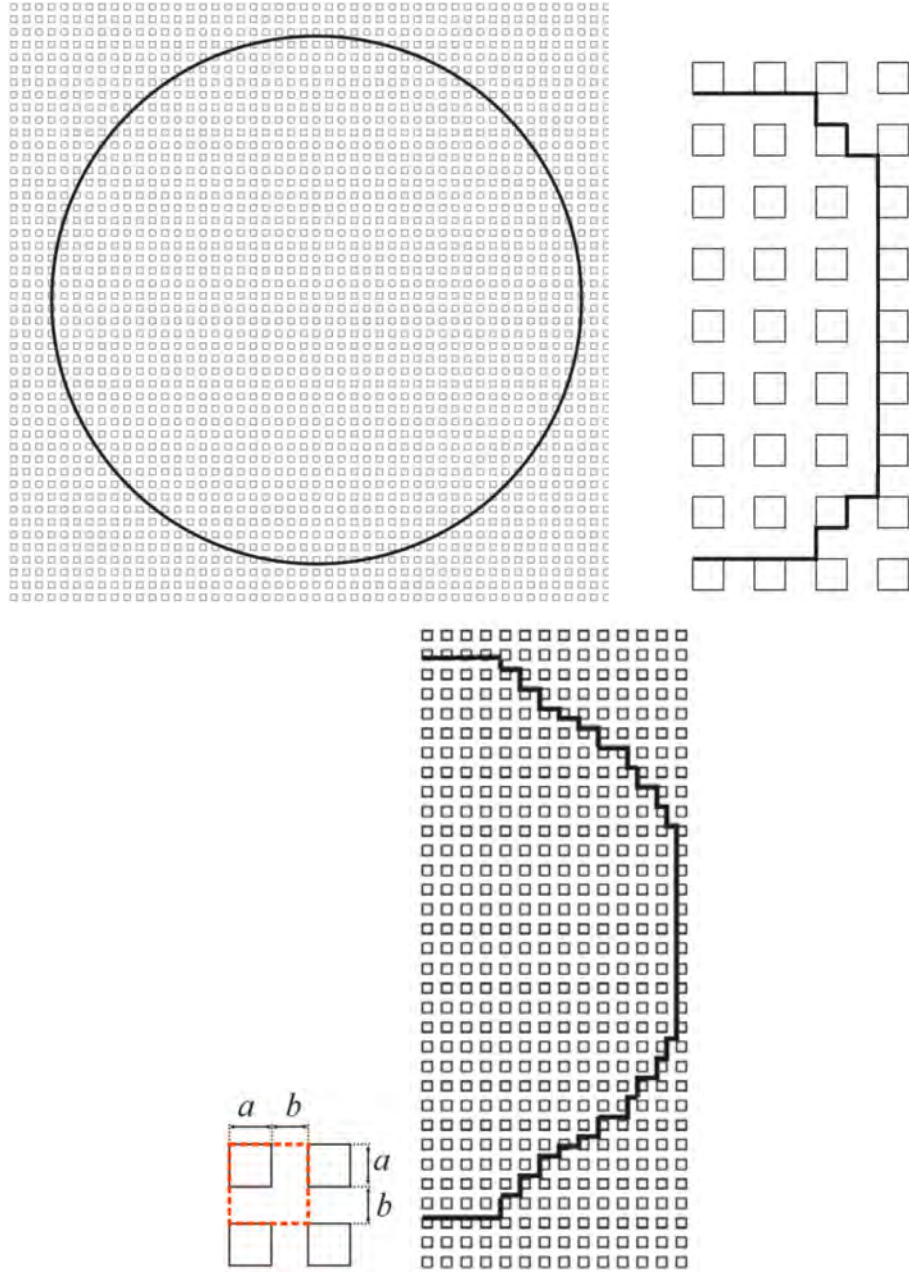


Figure 1. Schematic top views of drop DCL for the drop on a patterned surface with square post array (not to scale). (a) The inset shows the DCL shape on a large length scale microgeometrical surface. (b) DCL shape on a small length scale microgeometrical surface. Note that the dashed cells refer to the repetitive units.

To determine the value of local receding CA at the solid-liquid contact part ($\theta_{s,rec}$) in Eq. (6), a model of contact line retreating behaviour is introduced in Figure 2, similar to the models illustrated by Extrand⁷³ and Dorrer and Ruehe.³⁹ One can see that the drop exhibits a local receding CA equal to that on a smooth surface ($\theta_{s,0}$) when the contact line crosses the flat top of

the post. As the drop volume is decreasing, the drop contact line retreats to the post edge, and then is pinned. Theoretically, the contact line cannot move until the same local receding CA (θ_{r0}) on the side wall of the post is established. However, for composite state, the drop is suspended between two posts, and there is only one point pinned at the edge. The pinning point is so weak that it can be easily pinched off and depin from the edge before the local receding CA decreases to a small value. In fact, Extrand⁷³ even ignored such pinning for composite states, and treated $\theta_{s,rec}$ as a value equal to θ_{r0} .

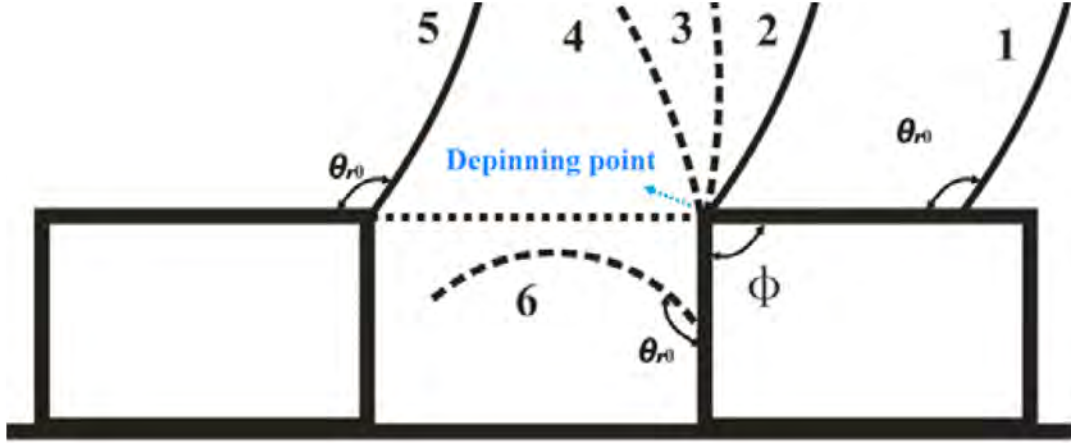


Figure 2. An enlarged side view near the receding contact line of a drop suspended on the posts: 1-2 the drop contact line is retreating on the flat post top with a local receding CA equal to that exhibited on the smooth surface (θ_{r0}); 3-4 the contact line is pinned on the edge; 5 a new contact point is formed on the nearest post after depinning happens at 4; 6 theoretical contact line movement with local receding CA (θ_{r0}) on the side of the post, which will unlikely happen on a hydrophobic post with the solid edge angle $\Phi=90^\circ$.

To determine the value of local advancing CA at the solid-liquid contact part $\theta_{s,adv}$ in Eq. (7), a model of the contact line advancing motion is shown in Figure 3, which is also similar to the models illustrated by Extrand⁷³ and Dorrer and Ruehe.³⁹ One can see that a drop exhibits a local advancing CA equal to that on a smooth surface (θ_{a0}) when the contact line crosses the flat top of the post. As the drop volume is increasing, the contact line continues to spread and finally reaches the post edge. Then, the contact line will be pinned on the post edge. Theoretically, until a CA of 180° is reached,³⁹ the meniscus near the contact point could then touch the next post and form a new contact point. As a result, the local advancing CA at the solid-liquid contact part appears to be $\theta_{s,adv} = 180^\circ$, and so the apparent advancing CA (θ_a) from Eq. (7), no matter what f is, can be calculated to be 180° . Based on the above analysis, Dorrer and Ruehe³⁹ claimed that the advancing contact angles remain unaffected ($\theta_a \sim 180^\circ$) as the microgeometrical parameters (f_a and S) are varied. However, this may not be the truth because the meniscus will fluctuate about its equilibrium position, depending on the external energy transferred from the environment, e.g., mechanical vibrations,⁷⁵⁻⁷⁷ and thus the drop may sense the nearest post and form a new contact point before $\theta_{s,adv}$ reaches 180° . So under a relatively stable environment with certain vibrational energy, the drops on surfaces with small post spacing can sense the nearest posts more easily than those on surfaces with large post spacing (for the same post width), indicating a smaller $\theta_{s,adv}$. However, $\theta_{s,adv}$ cannot be theoretically determined, since the vibrational energy from the

environment is unknown. The above speculations will be demonstrated based on experimental results in Section 4.

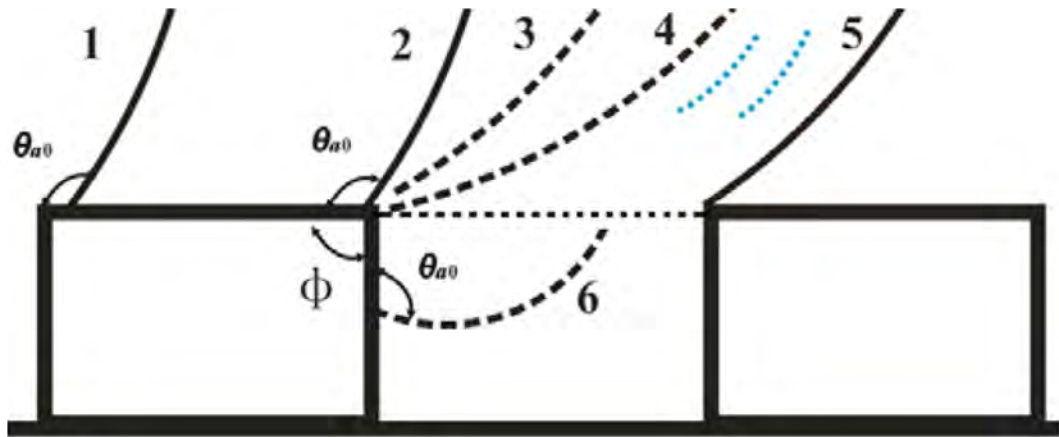


Figure 3. An enlarged side view near the advancing contact line of a drop suspended on the posts: 1-2 the drop contact line is propagating on the flat post top with an advancing CA equal to that exhibited on the smooth surface (θ_{a0}); 3-4 the contact line is pinned on the corner; 5 a new contact point is formed on the nearest post when the meniscus of 4 is oscillating around its equilibrium position; 6 theoretical contact line movement with advancing CA (θ_{a0}) on the side of the post, which will unlikely happen on a hydrophobic post with solid edge angle $\Phi=90^\circ$.

3 Experimental Methods

3.1 Experimental Design

Patterned surfaces with different post shapes, i.e., square, triangle, and circle, were designed. Figure 4 shows schematic depiction of repetitive unit cells for patterned surfaces with different microgeometries. The use of these simple geometrical shapes can allow us to control geometrical parameters conveniently. For example, solid area fraction f_a (for uniformly patterned rough surface, the global solid area fraction all over the surface is equal to the local solid area fraction in the region of DCL), characterized by the solid-liquid contact area fraction for composite states, is defined to be $a_1^2/(a_1+b_1)^2$, $0.43a_2^2/(a_2+b_2)^2$ and $0.79a_3^2/(a_3+b_3)^2$ for square, triangle and circle post arrays, respectively; microgeometrical length scale S , characterized by the top surface area of individual post, is defined to be a_1^2 , $0.43a_2^2$ and $0.79a_3^2$ for square, triangle and circle post arrays, respectively; edge length density P , characterized by the edge length per unit area, is defined to be $4a_1/(a_1+b_1)^2$, $3a_2/(a_2+b_2)^2$, $3.14a_3/(a_3+b_3)^2$ for square, triangle and circle post arrays, respectively. Note that the surface area (2-dimension) of individual post is more meaningful to be used as the indication of the microtexture length scale than any other parameters (e.g., the post width or post spacing), and it is especially useful for defining the length scale of different microgeometry shapes. Microgeometrical effects on wetting behaviour can be understood through the comparisons of surface wettability when the above geometrical parameters are precisely controlled. It is worth pointing out that in this report, composite states are mainly investigated, and as such solid area fraction is selected to be the controlled geometrical parameter rather than roughness parameter, r .^{38, 39, 71}

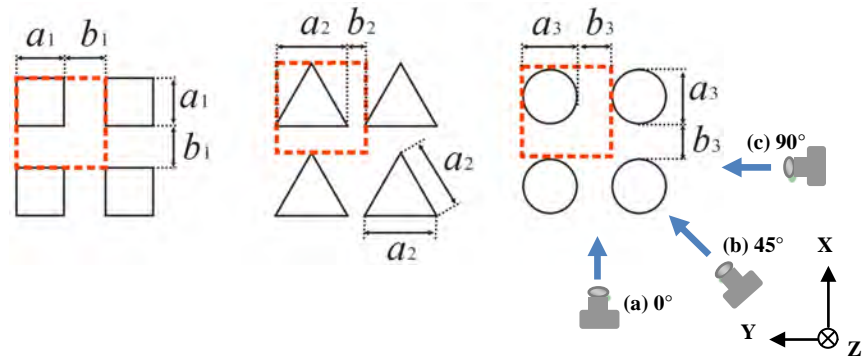


Figure 4. Schematic depiction of top views for patterned surfaces with different microgeometries. The dashed cells refer to the repetitive units. Images of drops sitting on the post arrays were taken from azimuthal angle of (a) 0° , (b) 45° and (c) 90° relative to x axis.

In order to investigate microgeometrical effects on wetting behaviour, the size of surface microgeometrical parameters are carefully designed, which have been given in Tables 1, 2 and 3. For features in each table, f_a and S for different microgeometries are kept constant, so wettability comparisons for surfaces of each table will show geometrical shape effect, e.g., the effect of P . Comparing features of Table 2 to features of Table 1, S is decreased by halving the post width (a) and spacing (b) for different pattern shapes while f_a is kept constant, so wettability comparison

between them will show length scale effect. Comparing features of Table 3 to features of Table 1, the post widths for different pattern shapes are all halved while the cell area $(a+b)^2$ are kept constant, so wettability comparison between Table 1 and Table 3 can show post size effect. In addition, comparing features of Table 3 to features of Table 2, f_a is decreased while S is kept constant, so wettability comparison between Table 2 and Table 3 can show post density effect. Note that two post heights 20 and 30 μm are set, which are sufficient for drops to stay in composite state as shown in Section 4.

Table 2. Theoretical settings for microgeometries ($f_a = 0.28$, $S = 256\mu\text{m}^2$). a , b and h represent the post width, spacing and height, respectively; f_a , r_w represent the solid area fraction and Wenzel's roughness, respectively; θ_C and θ_w represent the CAs from Cassie's and Wenzel's equations, respectively; P and S represent the edge length density and length scale, respectively; θ_Y is 111° which is assumed to be the average of advancing and receding CAs on smooth surface.

Pattern	a (μm)	b (μm)	h (μm)	f_a [θ_C ($^\circ$)]	r_w [θ_w ($^\circ$)]	P (μm^{-1})	S (μm^2)
Square	16	14	30	0.28(144.4)	3.13(180)	0.071	256
			20	0.28(144.4)	2.42(145.9)	0.071	256
Triangle	24.3	5.7	30	0.28(144.4)	3.43(180)	0.081	256
			20	0.28(144.4)	2.62(153.7)	0.081	256
Circle	18	12	30	0.28(144.4)	2.89(171.4)	0.063	256
			20	0.28(144.4)	2.26(140.6)	0.063	256

Table 3. Theoretical settings for microgeometries with smaller length scale ($f_a = 0.28$, $S = 64\mu\text{m}^2$)

Pattern	a (μm)	b (μm)	h (μm)	f_a [θ_C ($^\circ$)]	r_w [θ_w ($^\circ$)]	P (μm^{-1})	S (μm^2)
Square	8	7	30	0.28(144.4)	5.27(180)	0.14	64
			20	0.28(144.4)	3.84(180)	0.14	64
Triangle	12.2	2.8	30	0.28(144.4)	5.86(180)	0.16	64
			20	0.28(144.4)	4.24(180)	0.16	64
Circle	9	6	30	0.28(144.4)	4.78(180)	0.13	64
			20	0.28(144.4)	3.52(180)	0.13	64

Table 4. Theoretical settings for microgeometries smaller f_a ($f_a=0.071$, $S=64\mu\text{m}^2$)

Pattern	a (μm)	b (μm)	h (μm)	$f_a[\theta_C(\text{°})]$	$r_w[\theta_w(\text{°})]$	$P(\mu\text{m}^{-1})$	$S(\mu\text{m}^2)$
Square	8	22	30	0.071(162.4)	2.07(135)	0.036	64
			20	0.071(162.4)	1.71(125.8)	0.036	64
Triangle	12.2	17.8	30	0.071(162.4)	2.22(139.3)	0.041	64
			20	0.071(162.4)	1.81(128.3)	0.041	64
Circle	9	21	30	0.071(162.4)	1.95(131.7)	0.031	64
			20	0.071(162.4)	1.63(123.9)	0.031	64

3.2 Preparation of Patterned Silicon Substrates

All surface microgeometries described above are fabricated by lithography and reactive ion etching (RIE) techniques on pure silicon wafers covered by a 500nm thick silicon dioxide layer, which is schematically shown in Figure 5. Firstly, patterns of designed shapes were transferred from a photomask (NanoFab, University of Alberta) to a silicon dioxide layer on 4 in. (100)-orientation silicon wafers (P/B-doped, resistivity from 1 to 35 ohm-cm, thickness $525\pm25\mu\text{m}$, Silicon Valley Microelectronics, Inc.) by contact lithographic techniques (HPR 504 photoresist, ABM Mask Aligners) and reactive ion etching process (STS-RIE). The patterned silicon dioxide acted as a masking layer in the following Cryo process (Oxford ICP-RIE Cryo Etch), which produced an anisotropic etch in silicon. Etching depth or post height can be precisely controlled by etching time. When etching process was complete, holes were drilled in the center of each pattern ($1.5\text{cm}\times1.5\text{cm}$) by diamond micro-drills (MCDU30, diameter 0.762 mm, UKAM) to allow for mounting of a syringe below the surface to create a drop on top of the surface, see Figure 6. Then, the wafers were cleaned in deionized water, iso-propanol, and acetone in sequence. In order to ensure chemical homogeneity of surfaces, the patterned silicon wafers were kept in thermal oxidation tube at 900°C for 10 min to grow a 70nm thick silicon dioxide layers on the newly exposed silicon surfaces.

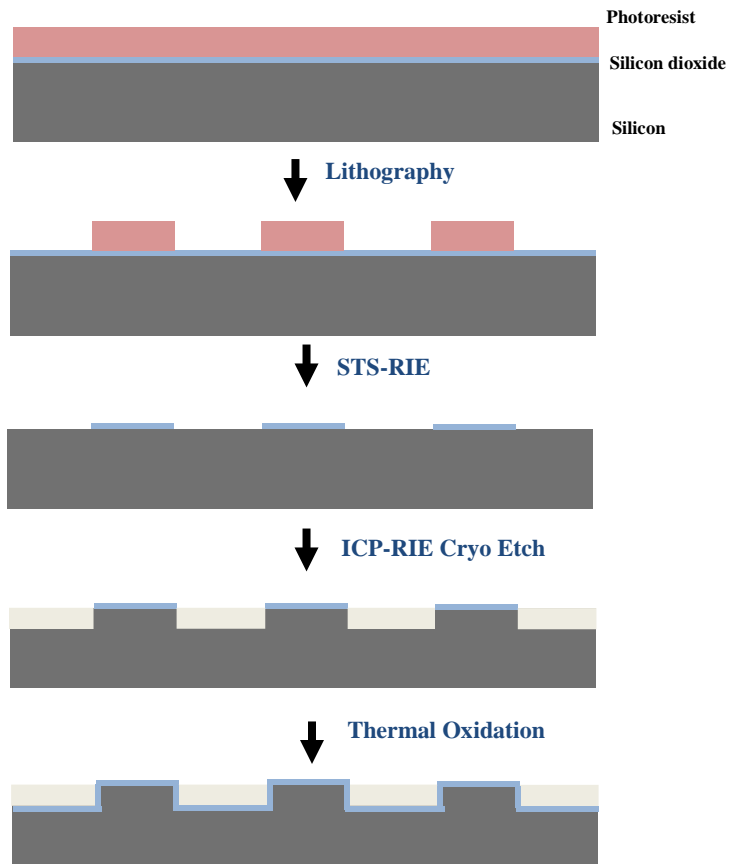


Figure 5. A schematic illustration for the micromachining procedure on silicon wafers. The thermal oxidation process is to ensure chemical homogeneity.

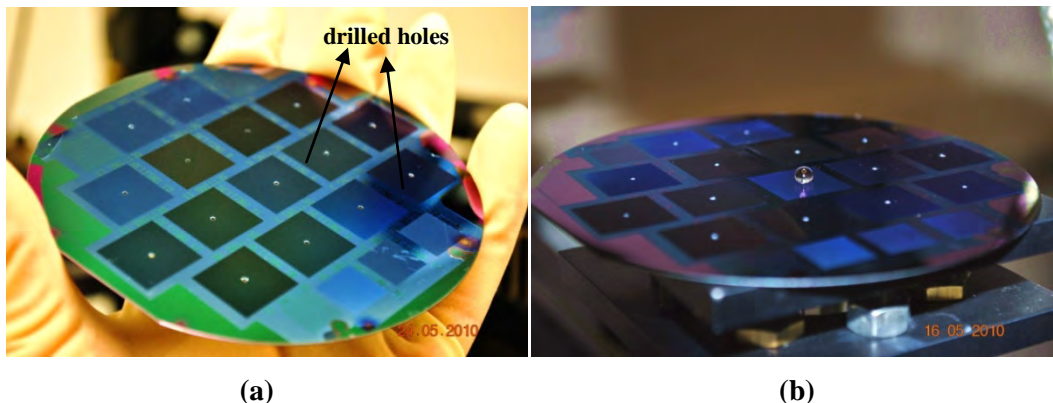


Figure 6. (a) A patterned silicon substrate by lithography and RIE techniques with drilled holes on. (b) A patterned silicon substrate mounted on the stage of a contact angle measuring system with syringe below to create a drop on top of the surface.

3.3 Surface Modification

The deposition cycle part of the Bosch process (Oxford Plasmalab ICP-RIE) was used to modify surface chemical property. Using C_4F_8 source gas, a chemically inert passivation layer (a substance similar to Teflon) was homogeneously coated on the patterned silicon surface. When the deposition time is set to be 90 sec., a 60 nm thick polymer film can be detected.

3.4 Surface Characterization

Scanning Electron Microscope (SEM-LEO 1430) and White Light Confocal Microscopy (LCM-CSM 700) were applied to check the dimensions of the microgeometries. All the data are given in the supporting information (A1, Annex A). Feature sizes within 5% deviation from the ideal sizes shown in Tables 1, 2 and 3 are accepted, since there is 7% system error during the micromachining and even in the dimensional measurement. The thickness of C_4F_8 passivation layer and silicon dioxide layer can be detected by a contact profilometer (Alphastep 200) and Filmetrics Resist and Dielectric Thickness Mapping System, respectively.

3.5 Contact Angle Measurements

A custom-built apparatus^{34, 78} was used for measuring advancing and receding CAs for the quasi-static advancing and receding contact line. A clean syringe filled with the deionized water was mounted under the silicon wafer, with the tip position just underneath the top of the hole, see Figure 6b. The syringe was driven by a motor at a rate of 0.5 $\mu\text{L/s}$ for the advancing and receding CAs measurements by adding and removing the water from the drop, which is low enough that inertial effects are minor. Side (from various azimuthal angles, see Figure 4) and top images of drops were recorded by two cameras. Drop image analysis programs were developed to determine the contact angles. Side images from azimuthal angles 0° to 170° were used to generate the DCL shape. Note that it is impossible to capture the DCL from the top view when the contact angle is larger than 90° .

4 Results and Discussion

The advancing (θ_a) and receding (θ_r) contact angles as well as contact angle hysteresis (CAH) for water on smooth silicon wafers untreated (SWU), treated (SWT) by thermal oxidation, and modified by C_4F_8 passivation are given in Table 5. Note that the Young's CA can be approximated to be the average of advancing and receding CAs. Figure 7 shows the water drop images sitting on smooth SWT before and after surface modification. One can see that a hydrophilic surface can be modified to be hydrophobic effectively by C_4F_8 passivation treatment.

Table 5. CA measurement on smooth silicon wafers. Silicon wafers untreated (SWU); silicon wafers treated (SWT) in 900°C (10min), SiO_2 thickness: 70nm; SWU + C_4F_8 passivation (90sec.), polymer thickness: 60nm; SWT + C_4F_8 passivation (90sec.), polymer thickness: 60nm. Note that SD is the standard deviation for measurements.

	θ_a (°) ± SD	θ_r (°) ± SD	CAH (°) ± SD
SWU	48.5±1.29	23.7±1.28	24.8±0.28
SWT	57.1±0.84	11.6±0.11	45.0±0.32
SWU + C_4F_8	123.4±0.06	99.3±1.05	23.8±0.61
SWT + C_4F_8	123.5±0.10	99.6±0.19	23.8±0.23

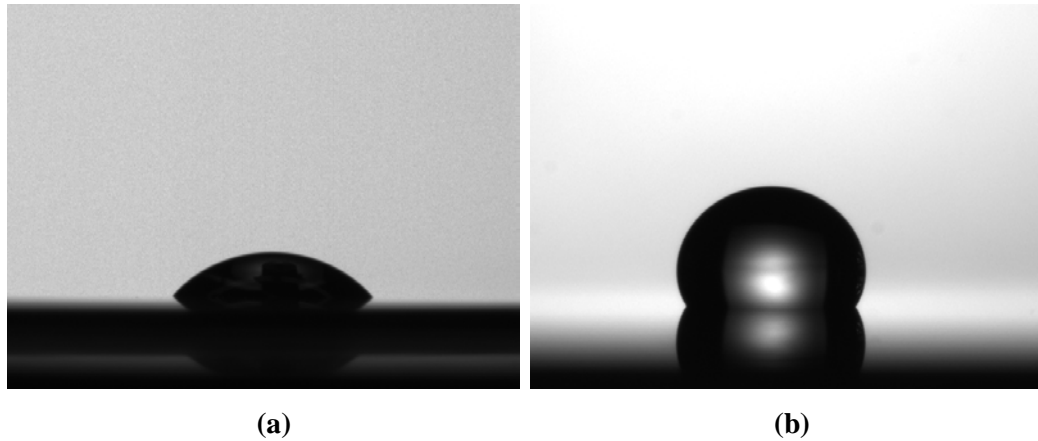


Figure 7. Images of water drops sitting on (a) smooth SWT surface; (b) smooth SWT surface treated by C_4F_8 passivation.

Figure 8 shows the SEM images of surfaces patterned with square, triangle and circle post arrays. The dimensions of post width, spacing and height measured by SEM and LCM are listed in the supporting information (A1, Annex A). The results show that the designed microgeometrical structures with required dimensions described in Tables 1, 2 and 3 have been successfully realized by the lithography and RIE technologies.

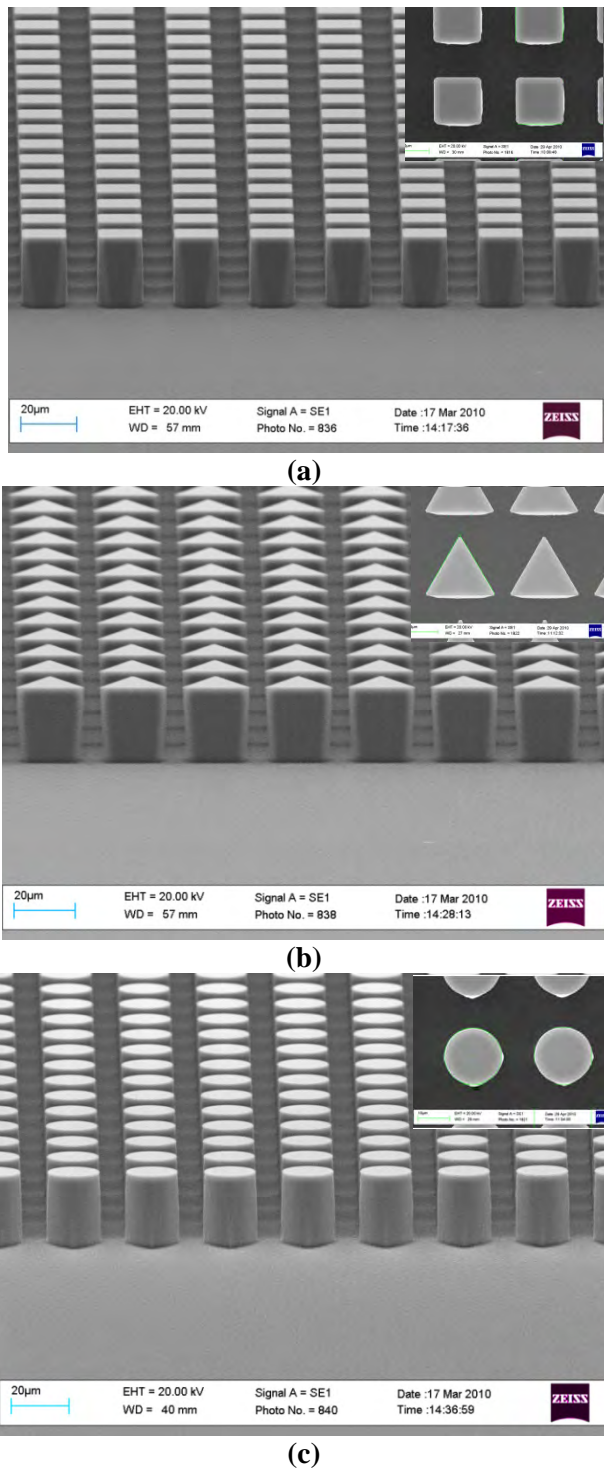


Figure 8. SEM images of the surfaces patterned with (a) Square posts, (b) Triangle posts and (c) circle posts for microstructures of Table 1, post height 30 µm. The insets show the top views of the microstructures with different post shapes.

4.1 Wetting on Hydrophilic Patterned Surfaces

Wetting behaviour on patterned surfaces before surface modification has been tested. Figure 9a shows the side views of a water drop spreading on the square post array (Table 1, post height=20 μm) from azimuthal angle of 0°. It is clear from the images that a liquid film inside the surface microstructures propagates faster than the drop (liquid is added by the syringe at a rate of 0.5 $\mu\text{L/s}$). Attempts to measure the contact angles failed because the water drop would all be absorbed into the microstructures to form the liquid film and CA was finally decreased to 0 degree. Bico *et al.*⁷⁹ derived a condition for such wetting phenomenon (they called it an intermediate between the ones for spreading and for imbibition) to happen,

$$\theta_Y < \theta_{\text{critical}} \cos \theta_{\text{critical}} = (1 - f)/(r - f) \quad (10)$$

In our case, the Young's CA (θ_Y equals to 34.3°, the average of advancing and receding CAs on smooth surface) is smaller than the critical CA (θ_{critical} equals to 70.3°) (from Table 1, $f_a=0.28$, $r=2.42$), and so the condition shown in Eq. (10) is satisfied. In particular, a rectangular spreading shape has been observed from the top views (Figure 9b). Interestingly, the same rectangular spreading pattern has been seen on the other microgeometrical surfaces, regardless of the microgeometrical shapes, i.e., square, triangle and circle post arrays (Tables 1, 2 and 3 with post heights 20 and 30 μm). The results reveal that the spreading speed of liquid film on patterned surfaces with tetragonally arrayed posts along x and y axis are slower than that along the diagonal directions regardless of what post shape it is. Dorrer and Ruehe⁸⁰ have observed a similar wetting phenomenon on hydrophilic square post arrays.

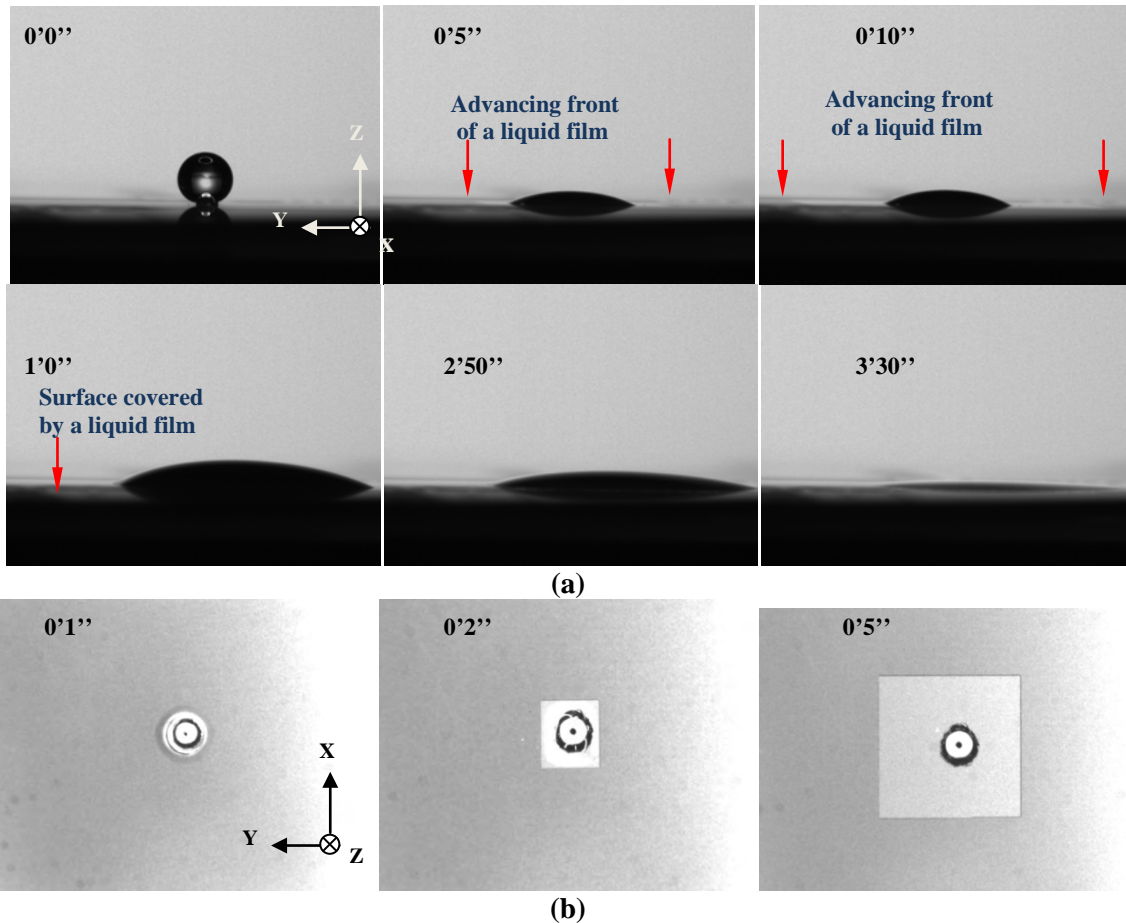


Figure 9. (a) Side and (b) top views for water drop on the square post array (Table 1, post height=20 μm) before surface modification. Note that the syringe is underneath the drop through the hole. The insets show the time sequence.

4.2 Wetting on Hydrophobic Patterned Surfaces

Figure 10 shows that water drop can sit on top of posts for the patterned surface after surface modification. Light can penetrate through the post spacing underneath the drop, indicating air entrapment and composite wetting state.

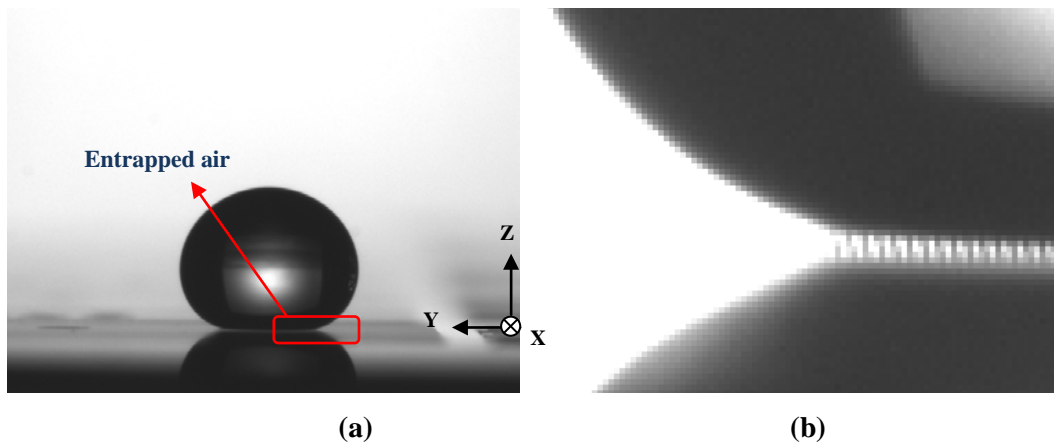


Figure 10. (a) Water drop sitting on the patterned surface. (b) A partial enlargement at the three phase contact point which is artificially magnified by three times. Note that light can penetrate through the post spacing (square post array of Table 3 with height 30 μ m).

4.2.1 CAs from Azimuthal Angle of Zero Degree

Comparison of variations of apparent drop advancing and receding CAs with respect to pattern types and geometrical parameters are shown in Figure 11, measured from 0 degree azimuthal angle (original CA data has been given in supporting information A2, Annex A). Student's t-test has been applied for the comparison of CA values discussed below. One can see that despite some errors generated by the light penetration mentioned above, for different post heights (Figure 11a and b), contact angles almost show the same trend. As a result, only the CA data for microgeometries with post height 20 μ m (Table A2-1) has been applied for analysis below.

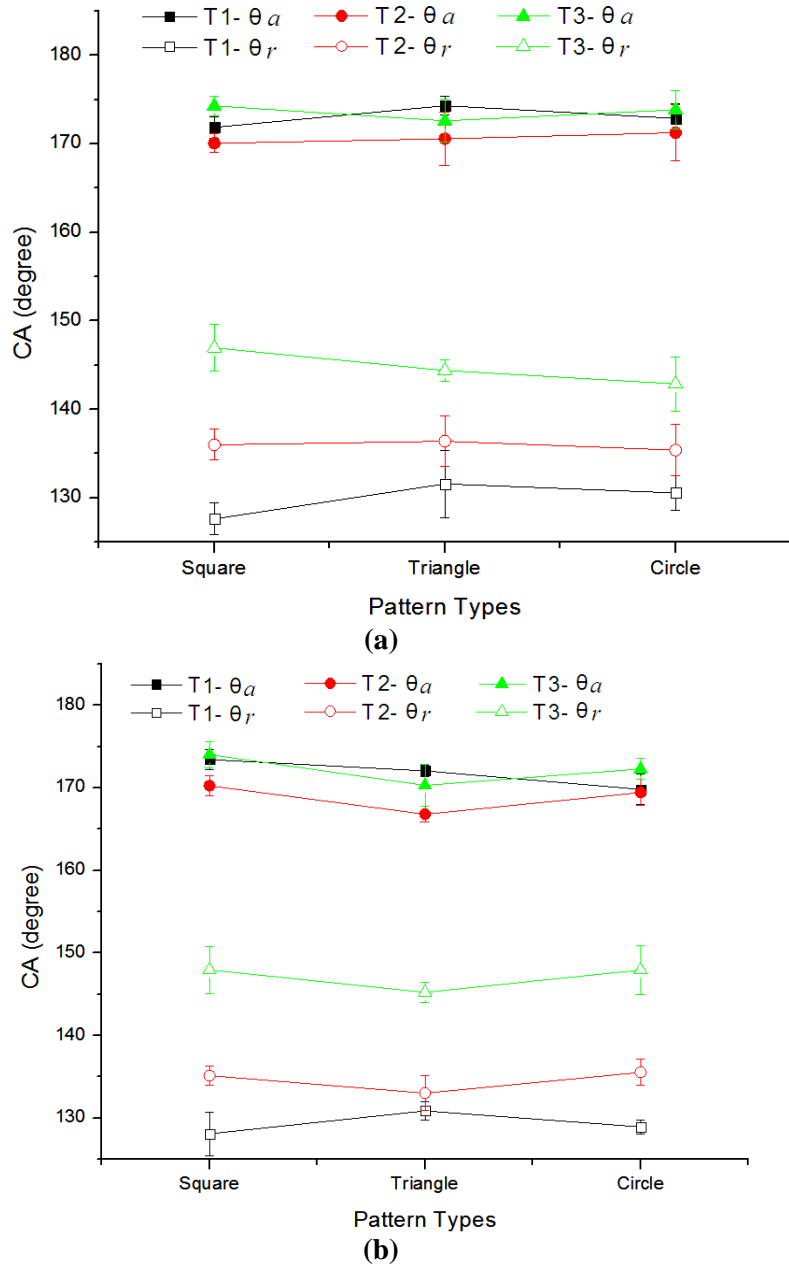


Figure 11. Variations of advancing (θ_a) and receding (θ_r) contact angles with respect to pattern types and geometrical parameters corresponding to Tables 1 (T1: $f_a = 0.28$, $S = 256\mu\text{m}^2$), 2 (T2: $f_a = 0.28$, $S = 64\mu\text{m}^2$) and 3 (T3: $f_a = 0.071$, $S = 64\mu\text{m}^2$) (a) for post height 20 μm and (b) post height 30 μm . Note that the CAs were measured from azimuthal angle of 0 degree.

4.2.1.1 Receding CA Analysis

Comparing the apparent receding CAs on patterned surfaces with microgeometrical parameters given in Tables 1 ($f_a = 0.28$, $S = 256\mu\text{m}^2$) and 1.2 ($f_a = 0.28$, $S = 64\mu\text{m}^2$), a quite different wetting behaviour can be observed though f_a has been fixed, see Figure 11a and Table A2-1. Taking the square post arrays for example, the apparent receding CA (θ_r) for the microtexture of Table 1 ($\theta_r = 127.6^\circ$, $f_{real} = 0.47$, $f_l = 0.53$, $f_a = 0.28$, $S = 256\mu\text{m}^2$) is much smaller than that for the microtexture of Table 2 ($\theta_r = 136.0^\circ$, $f_{real} = 0.34$, $f_l = 0.53$, $f_a = 0.28$, $S = 64\mu\text{m}^2$), showing a strong dependence on the length scale S ; note that f_{real} is calculated by substituting θ_r in Eq.(6) and given in Table A2-1, and the local solid linear fraction f_l for square post array is obtained from Eq. (9). The same phenomenon can be observed in Dorrer's data:³⁹ for the patterned surfaces with the same f_l and f_a , the apparent receding CA will increase (so the real local contact fraction f_{real} will decrease) dramatically when the length scale S decreases. In particular, it is found that the value of f_{real} is always located between f_l and f_a , and f_{real} decreases from a value close to f_l to a value close to f_a when S decreases. In order to better understand the dependence of f_{real} on S , it is useful to establish theoretical relationship between them. Based on the experimental data of apparent receding CAs from ours and Dorrer's,³⁹ we propose a phenomenological correlation as:

$$f_{real} = f_l(1 - e^{-S/A}) + f_a e^{-S/A} \quad (11)$$

where S is the length scale and A (μm^2) is a fitting parameter based on experimental data. Combining Eqs. (6) and (11), a theoretical relationship between the apparent receding CA (θ_r) and length scale (S) can be established. Figure 12 shows the comparison between the experimental apparent receding CA data and theoretically predicted apparent receding CAs. As seen, the predicted apparent receding CAs are quite consistent with the experimental data. Therefore, a quantitative correlation between apparent receding CA and length scale has been successfully established. It is worth pointing out that from Eq. (11), a maximum receding CA can be reached when S approaches 0 (f_{real} approaches f_a), i.e., a small S is favoured for water-repellent rough surfaces. This may be one of the reasons that needle-like structure⁸¹ is usually preferred for constructing superhydrophobic surfaces.

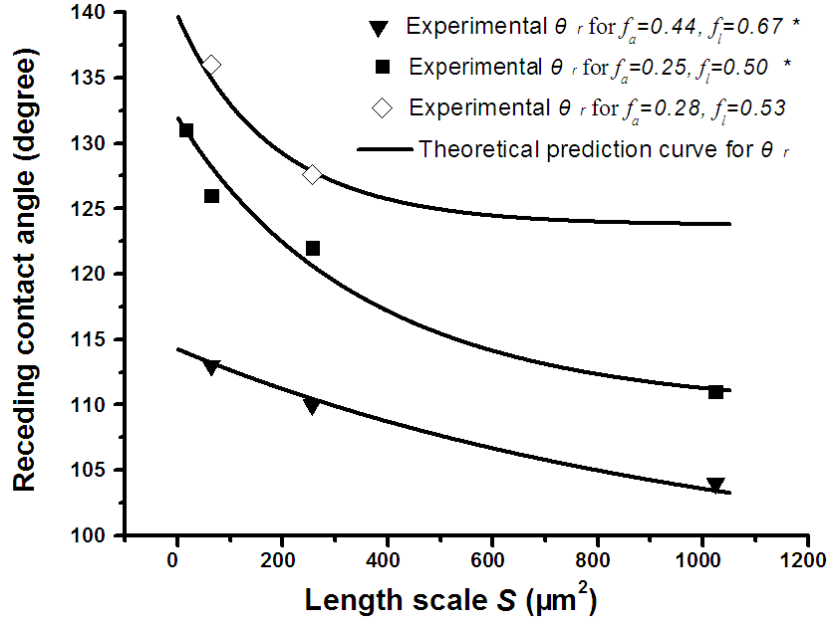


Figure 12. The comparison between the experimental apparent receding CA data and theoretically predicted apparent receding CAs for square post arrays. Note that the experimental data noted by symbol * is from Dorrer's experiment.³⁹

Comparing with the f_{real} values (calculated from the experimental data θ_r , see Table A2-1) for surfaces of Tables 1 and 2 ($f_a=0.28, f_l=0.53$), the f_{real} for surfaces of Table 3 ($f_a=0.071, f_l=0.27$) own a much smaller value (see supporting information S2, Annex A). Based on Eq. (11), such phenomenon can be attributed to the great decrease of both local solid area ($f_a=0.071$) and local solid linear ($f_l=0.27$) fractions.

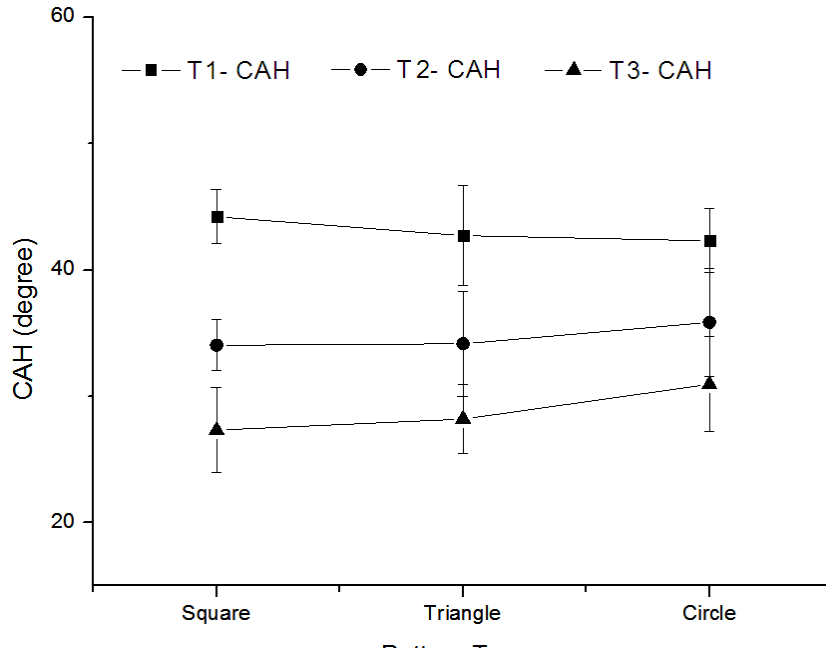
In addition, for each of the studied surfaces of each table (Tables 1, 2 and 3) with different microgeometrical shapes (square, triangle and circle) but the same f_a and S values, the receding CAs have shown some minor differences. From Eq. (11), we can attribute the minor difference to the different solid linear fraction f_l for varied post shapes. Unless a detailed DCL profile is gained for drop on triangle and circle post arrays, it is impossible to theoretically determine the value of f_l as well as f_{real} , though experimental f_{real} for triangle and circle post arrays show values approximate to that for square post array, see Table A2-1.

4.2.1.2 Advancing CA Analysis

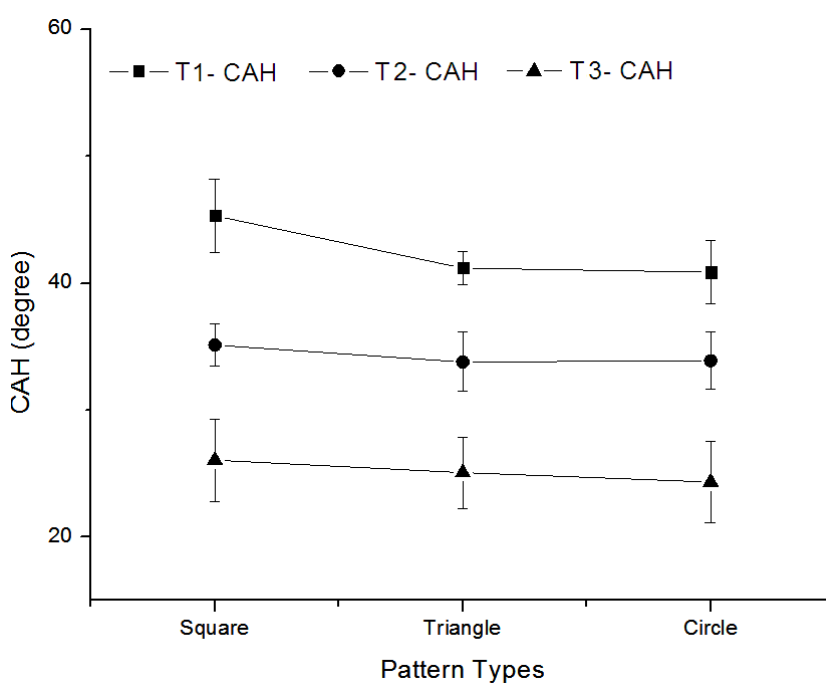
Unlike the apparent receding CA, the apparent advancing CA is difficult to be predicted by Eqs. (7) and (11), since the local advancing CA ($\theta_{s,adv}$) in Eq. (7) at the solid-liquid contact part cannot be theoretically determined as discussed in Section 2.1.2. However, based on the experimental apparent advancing CA results, $\theta_{s,adv}$ can be calculated by Eq. (7) for all the patterned surfaces, see Table A2-1. Note that f_{real} in Eq. (7) at the advancing DCL is assumed to be equal to that at the receding DCL for axisymmetric post shapes. By comparing $\theta_{s,adv}$ between patterned surfaces with various microgeometrical parameters, the edge pinning effect for the advancing contact line at the microgeometrical edge can be revealed. For example, comparing $\theta_{s,adv}$ for square post array

of Table 2 ($\theta_{s,adv}=162.8^\circ$, $a=8 \mu\text{m}$, $b=7 \mu\text{m}$, $h=20 \mu\text{m}$) and Table 3 ($\theta_{s,adv}=167^\circ$, $a=8 \mu\text{m}$, $b=22 \mu\text{m}$, $h=20 \mu\text{m}$), it can be seen that $\theta_{s,adv}$ shows a smaller value for the one with small post spacing (surface of Table 2) than that with large post spacing (surface of Table 3), which is consistent to the speculations for the pinning property of advancing contact line discussed in Section 2.1.2; i.e., for the same post width, small post spacing can induce a smaller $\theta_{s,adv}$. Comparing $\theta_{s,adv}$ for square post array of Table 1 ($\theta_{s,adv}=168.1^\circ$, $a=16 \mu\text{m}$, $b=14 \mu\text{m}$, $h=20 \mu\text{m}$) with those for square post arrays of Table 2 and Table 3, it is observed that $\theta_{s,adv}$ for square post array of Table 1 shows the largest $\theta_{s,adv}$, indicating that not only a large post spacing, but a large post width can also induce a strong advancing contact line pinning effect. Interestingly, the same trend can be found for triangle and circle post arrays, respectively (see Table A2-1). In addition, we tried to compare $\theta_{s,adv}$ between post arrays with different post shapes in each Table (Tables 1, 2 and 3), however, no clear trend can be observed.

Figure 13 shows variations of CAH with respect to microgeometrical shapes and geometrical parameters corresponding to Tables 1, 2 and 3. Because CAH is the result of the difference of θ_a and θ_r , there is a direct relation between the variations of CAH and variations of θ_a and θ_r . Due to the much less pronounced variation of θ_a than variation of θ_r , CAH shows a very similar trend to θ_r .



(a)



(b)

Figure 13. Variations of CAH with respect to pattern types and geometrical parameters corresponding to Tables 1 (T1: $f_a = 0.28$, $S = 256\mu\text{m}^2$), 2 (T2: $f_a = 0.28$, $S = 64\mu\text{m}^2$) and 3 (T3: $f_a = 0.071$, $S = 64\mu\text{m}^2$) (a) for post height 20 μm and (b) post height 30 μm . Note that the CAs were measured from azimuthal angle of 0 degree.

4.2.1.3 CAs from other Azimuthal Angles

It is noted that wetting conditions can be different if it is observed from various directions even for the same patterned surface, see Figure 4. For square and circle post arrays, the same post and plane symmetries can be seen from azimuthal angles 0° and 90° , respectively; different post and plane symmetries can be seen from azimuthal angles 0° and 45° for square; the same post symmetry but different plane symmetry can be seen from azimuthal angles 0° and 45° for circle post arrays. Accordingly, CAs are measured from azimuthal angles 0° and 45° for square and circle post arrays, respectively. For triangle post arrays, post and plane conditions become asymmetric and extremely complex from azimuthal angles 45° , which can be confusing for investigation of microgeometrical effect. Though post and plane are still asymmetric from azimuthal angle of 90° , the post array is more regular than that from 45° . Therefore, CAs are measured from 90° for triangle post array.

Table 5 shows the CA results measured from various azimuthal angles for microgeometries of Table 1 (post height 20 μm). One can see that for square and circle post arrays, there is a large increase of receding CAs when the azimuthal angle changes from 0° to 45° . To make our explanation easily understandable, schematic illustrations of two columns of square post arrays as well as the DCL pinned at the rear post edge from the two azimuthal angles are shown in Figure 14. Similar to the analysis in Section 4.2.1, the apparent receding CA can be determined by the real local solid-liquid contact fraction f_{real} which is related to f_a , f_l and S (Eq. (6) and Eq. (11)). For square post arrays observed from 0° and 45° , they have the same f_a and S . However, f_l at the receding DCL from azimuthal angle 45° will be smaller than that from azimuthal angle 0° (0.53); note that though f_l from azimuthal angle 45° is difficult to be quantified due to the lack of knowledge of the exact position for receding DCL, it can be estimated to have a value smaller than 0.53 by a simple geometrical analysis. As a result, a smaller f_{real} and a larger receding CA can be obtained for azimuthal angle 45° than that for 0° . In addition, the local advancing CA in the solid-liquid contact part ($\theta_{s,adv}$) can be calculated from Eq. (7) based on the experimental data, see Table 6. One can see that $\theta_{s,adv}$ for square post array observed from 45° ($\theta_{s,adv} = 166.0^\circ$) is smaller than that from 0° ($\theta_{s,adv} = 168.1^\circ$), due to the smaller column spacing observed from angle 45° ($=0 \mu\text{m}$) than that from 0° ($=14 \mu\text{m}$), which is consistent with the advancing CA analysis in Section 4.2.1.

Table 6. CA Measurement on Patterned Surfaces from Various Azimuthal angles (For Microgeometries of Table 1, Post height=20 μ m); note that SD is the standard deviation for measurements.

	$\theta a(^{\circ})$	SD- θa	$\theta r(^{\circ})$	SD- θr	CAH($^{\circ}$)	SD-CAH	f_{real} from θr	$\theta_{s,adv}(^{\circ})$
Square-0 $^{\circ}$	171.9	1.19	127.6	1.79	44.2	2.15	0.47	168.1
Square-45 $^{\circ}$	171.6	1.84	134.3	1.91	37.3	2.66	0.36	166.0
Circle-0 $^{\circ}$	172.9	1.62	130.6	1.95	42.3	2.53	0.42	169.0
Circle-45 $^{\circ}$	170.4	1.52	134.6	1.17	35.8	1.92	0.36	163.9
Triangle-0 $^{\circ}$	174.3	1.08	131.6	3.81	42.7	3.96	0.40	171.0
Triangle-90 $^{\circ}$ - right	175.4	1.84	130.6	2.30	44.9	2.95	0.42	/
Triangle-90 $^{\circ}$ - left	172.6	1.81	131.9	1.32	40.8	2.24	0.40	/

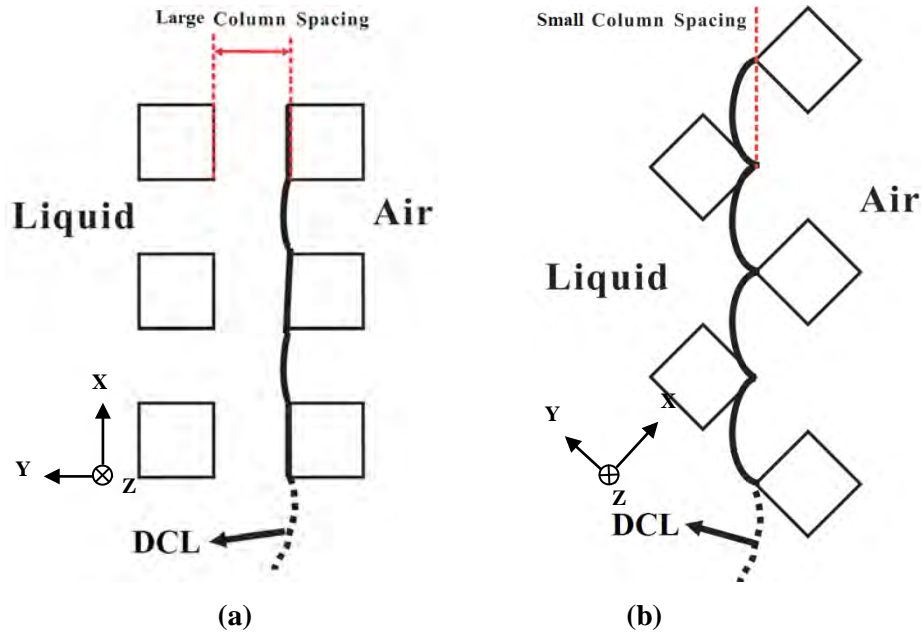


Figure 14. Schematic top views of two square post columns from azimuthal angles (not to scale) (a) 0 degree and (b) 45 degree. Note that the shapes of contact line are shown when the DCLs reach the post edges.

Schematic top views of two circle post columns from azimuthal angles 0 $^{\circ}$ and 45 $^{\circ}$ have been shown in Figure 15. Receding CA is much larger for azimuthal angle 45 $^{\circ}$ than that for 0 $^{\circ}$, attributing to the decreased f_{real} (similar to the above analysis for square post arrays); note that though f_{real} from both azimuthal angles of 0 $^{\circ}$ and 45 $^{\circ}$ are difficult to be quantified due to the lack of knowledge of the exact position for receding DCL, it can be estimated that f_{real} from the

azimuthal angle 45° is smaller than that from 0° by simple geometrical analysis, see Figure 15. In addition, $\theta_{s,adv}$ for circle post array observed from 45° ($\theta_{s,adv} = 163.9^\circ$) is smaller than that from 0° ($\theta_{s,adv} = 169.0^\circ$), due to the smaller column spacing observed from 45° ($=3.21 \mu\text{m}$) than that from 0° ($=12 \mu\text{m}$).

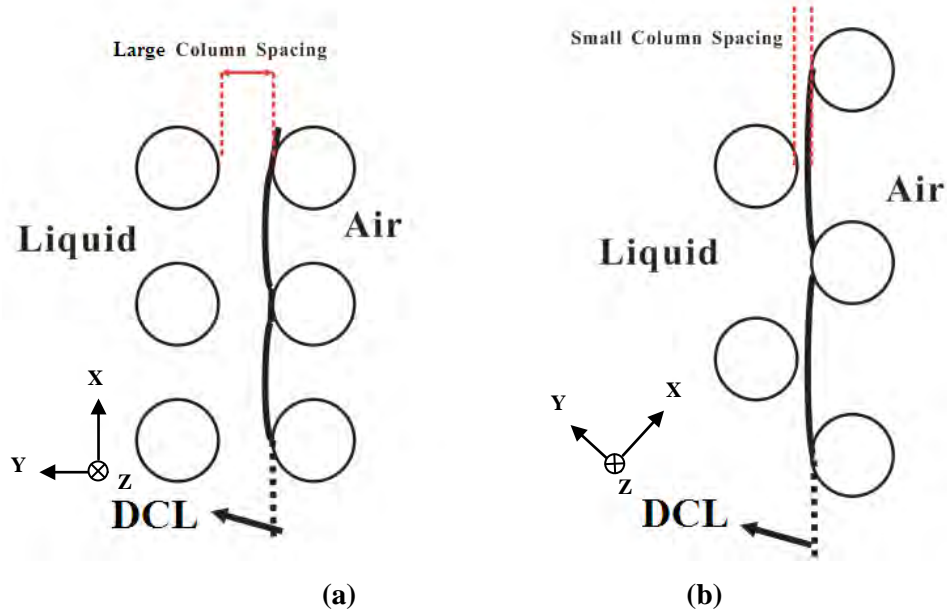


Figure 15. Schematic top views of two circle post columns from azimuthal angles (not to scale)
(a) 0° degree and (b) 45° degree. Note that the shapes of contact line are shown when the drop DCLs reach the post edges.

The wetting behaviour becomes more complex for triangle post array when it is observed from 90° . Since the drop DCL of the left side and right side have different wetting conditions (Figure 16), the advancing and receding CAs should be measured separately for the two sides. From Table 5, it is noted that the receding CA for the left side is larger than that for the right side when it is observed from 90° . This happens because f_{real} (similar to the above analysis for square post arrays) at the receding DCL for the left side ($L4$) is smaller than that for the right side ($L1$), implying a larger θ_r for the left side than that for the right side; note that though f_{real} at the left side is difficult to be quantified due to the lack of knowledge of the exact position for receding DCL ($L4$), it can be estimated to have a value smaller than that on the right side by simple geometrical analysis. For the advancing CA, because the assumption of f_{real} at the receding DCL is equal to that at the advancing DCL cannot be made for nonaxisymmetric post shape (Y axis), $\theta_{s,adv}$ cannot be obtained and compared. However, f_{real} at the advancing DCL on the right side ($L3$) can be estimated to have a value much smaller than that on the left side ($L6$), and in the meantime, a larger apparent advancing CA can be observed on the right side ($\theta_a = 175.4^\circ$) than that on the left side ($\theta_a = 172.6^\circ$), indicating a less important role of $\theta_{s,adv}$ in affecting θ_a in this case.

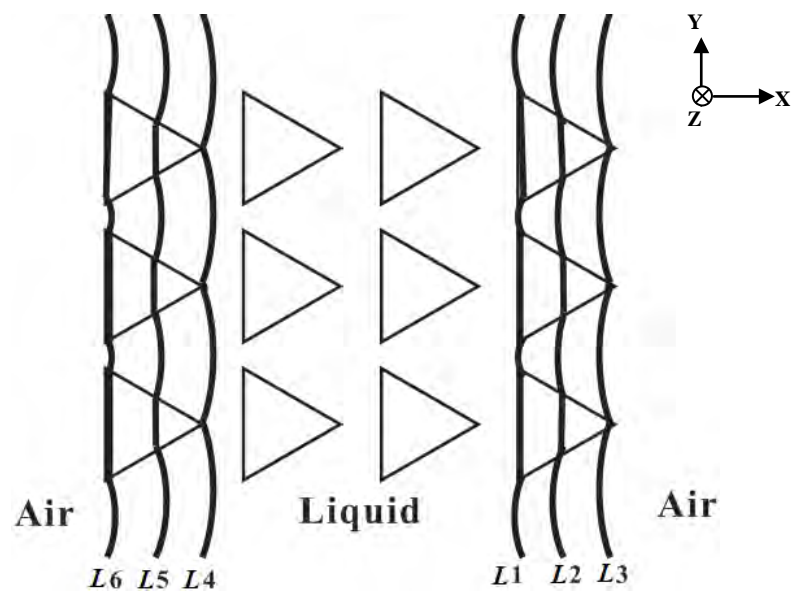


Figure 16. Schematic top view of triangle post array from azimuthal angle of 90 degree. *L₁*, *L₂* and *L₃* represent the DCL at the right side of the drop; *L₄*, *L₅* and *L₆* represent DCL at the left side of the drop.

5 Conclusions

In this study, patterned surfaces with three microgeometry arrays (square, triangle and circle) have been obtained by micro/nanofabrication techniques. Wetting behaviour of water drops on those surfaces has been systematically investigated. An intermediate wetting state between spreading and imbibition has been observed on microstructured hydrophilic silicon surfaces. After surface modification by C_4F_8 passivation, water drops can sit on top of the microgeometrical posts and show superhydrophobicity. Several important effects of microgeometries on the wetting behaviour have been discussed, i.e., length scale effect, edge and corner pinning effect, geometrical shape effect, direction-dependent effect, etc. In particular, for the micropatterned surfaces with the same solid area fraction, the advancing CA is found to have a slight decrease with the reduction of the length scale, due to the oscillation of the meniscus near the DCL; the receding CA is found to have a value between the CAs calculated by solid area fraction and solid linear fraction, depending on the microgeometrical length scale. In addition, CA results from different azimuthal angles reveal that wettability has a strong dependence on the orientation. For one patterned surface, the difference of edge/corner pinning effect in different directions can influence the receding CAs greatly. Furthermore, a drop can even exhibit an anisotropic wetting property from one azimuthal angle, depending on the microgeometrical shape, e.g., triangle post array. By designing the microgeometries on the patterned surfaces, a tunable wettability or a controlled drop wetting behaviour can be achieved.

6 Future Works

More study is needed for understanding microgeometrical effects on surface wettability, as listed below:

1. Measurement of adhesion force needed for peeling droplets off the patterned surfaces. The adhesion force can be considered as one of the criterion for the evaluation of hydrophobicity of the surfaces.¹³ Such force can be measured by a surface tension measurement with high sensitivity.
2. Investigation of edge energy related to the pinning effect of the contact line at the microgeometrical edge. This is important to the stability of Cassie's state/composite state. For patterned surfaces designed with the same solid area fraction, the contact line density P (see Tables 1, 2 and 3), i.e., the length of the asperity perimeter per unit area that could potentially suspend a liquid drop,⁷³ are distinct for different length scale or different post shape array surfaces (square, triangle and circle shape). Thus, different edge energy can be generated and so the stability of Cassie's state can strongly depend on the post length scale and the post shape.
3. Perhaps 3-D simulation for the contorted drop contact line by Surface Evolver.

References

- [1] Herminghaus, S.; Brinkmann, M.; Seemann, R. *Ann. Rev. Mater. Res.* **2008**, *38*, 101-121.
- [2] Bonn, D.; Eggers, J.; Indekeu, J.; Meunier, J.; Rolley, E. *Rev. Mod. Phys.* **2009**, *81*, 67.
- [3] Genzer, J.; Bhat, R. R. *Langmuir* **2008**, *24*, 2294-2317.
- [4] Morgenthaler, S.; Zink, C.; Spencer, N. D. *Soft Matter* **2008**, *4*, 419-434.
- [5] Hong, X.; Gao, X.; Jiang, L. *J. Am. Chem. Soc.* **2007**, *129*, 1478-1479.
- [6] Zhao, Y.; Lu, Q.; Li, M.; Li, X. *Langmuir* **2007**, *23*, 6212-6217.
- [7] Chen, Y.; He, B.; Lee, J.; Patankar, N. A. *J. Colloid Interface Sci.* **2005**, *281*, 458-464.
- [8] Sandre, O.; Gorre-Talini, L.; Ajdari, A.; Prost, J.; Silberzan, P. *Phys. Rev. E* **1999**, *60*, 2964-2972.
- [9] Zhu, L.; Feng, Y.; Ye, X.; Zhou, Z. *Sens. Actuators, A* **2006**, *A130-A131*, 595-600.
- [10] Shastry, A.; Case, M. J.; Boehringer, K. F. *Langmuir* **2006**, *22*, 6161-6167.
- [11] Su, Y.; Ji, B.; Zhang, K.; Gao, H.; Huang, Y.; Hwang, K. *Langmuir* **2010**, *26*, 4984-4989.
- [12] Cheng, Z.; Gao, J.; Jiang, L. *Langmuir* **2010**.
- [13] Lai, Y. K.; Gao, X. F.; Zhuang, H. F.; Huang, J. Y.; Lin, C. J.; Jiang, L. *Adv. Mater.* **2009**, *21*, 3799-3803.
- [14] Barthlott, W.; Neinhuis, C. *Planta* **1997**, *202*, 1-8.
- [15] Neinhuis, C.; Barthlott, W. *Ann. Bot.* **1997**, *79*, 667-677.
- [16] Koch, K.; Bhushan, B.; Jung, Y. C.; Barthlott, W. *Soft Matter* **2009**, *5*, 1386-1393.
- [17] Koch, K.; Bhushan, B.; Barthlott, W. *Prog. Mater. Sci.* **2009**, *54*, 137-178.
- [18] Bohn, H. F.; Barthlott, W. *Langmuir* **2009**.
- [19] Koch, K.; Bhushan, B.; Barthlott, W. *Soft Matter* **2008**, *4*, 1943-1963.
- [20] Zheng, Y.; Gao, X.; Jiang, L. *Soft Matter* **2007**, *3*, 178-182.
- [21] Lee, W.; Jin, M. K.; Yoo, W. C.; Lee, J. K. *Langmuir* **2004**, *20*, 7665-7669.
- [22] Gao, X.; Jiang, L. *Nature* **2004**, *432*, 36.

- [23] Hu, D. L.; Chan, B.; Bush, J. W. M. *Nature* **2003**, *424*, 663-666.
- [24] Feng, X.-Q.; Gao, X.; Wu, Z.; Jiang, L.; Zheng, Q.-S. *Langmuir* **2007**, *23*, 4892-6.
- [25] Gao, X.; Yan, X.; Yao, X.; Xu, L.; Zhang, K.; Zhang, J.; Yang, B.; Jiang, L. *Adv. Mater. (Weinheim, Ger.)* **2007**, *19*, 2213-2217.
- [26] Zheng, Y.; Bai, H.; Huang, Z.; Tian, X.; Nie, F.-Q.; Zhao, Y.; Zhai, J.; Jiang, L. *Nature* **2010**, *463*, 640-643.
- [27] Garrod, R. P.; Harris, L. G.; Schofield, W. C. E.; McGettrick, J.; Ward, L. J.; Teare, D. O. H.; Badyal, J. P. S. *Langmuir* **2007**, *23*, 689-693.
- [28] Zhai, L.; Berg, M. C.; Cebeci, F. C.; Kim, Y.; Milwid, J. M.; Rubner, M. F.; Cohen, R. E. *Nano Letters* **2006**, *6*, 1213-1217.
- [29] Parker, A. R.; Lawrence, C. R. *Nature* **2001**, *414*, 33-34.
- [30] Zhang, X.; Shi, F.; Niu, J.; Jiang, Y.; Wang, Z. *J. Mater. Chem.* **2008**, *18*, 621-633.
- [31] Roach, P.; Shirtcliffe, N. J.; Newton, M. I. *Soft Matter* **2008**, *4*, 224-240.
- [32] Wenzel, R. N. *J. Ind. Eng. Chem.* **1936**, *28*, 988-994.
- [33] Cassie, A. B. D.; Baxter, S. *Trans. Faraday Soc.* **1944**, *40*, 546-551.
- [34] Pierce, E.; Carmona, F. J.; Amirfazli, A. *Colloids Surf., A* **2008**, *323*, 73-82.
- [35] Johnson, R. E., Jr.; Dettre, R. H. *Adv. Chem. Ser.* **1964**, *43*, 112-135.
- [36] Li, W.; Amirfazli, A. *J. Colloid Interface Sci.* **2005**, *292*, 195-201.
- [37] Dorrer, C.; Ruehe, J. *Soft Matter* **2009**, *5*, 51-61.
- [38] Oner, D.; McCarthy, T. J. *Langmuir* **2000**, *16*, 7777-7782.
- [39] Dorrer, C.; Ruehe, J. *Langmuir* **2006**, *22*, 7652-7657.
- [40] Gao, L.; McCarthy, T. J. *Langmuir* **2007**, *23*, 3762-3765.
- [41] McHale, G. *Langmuir* **2007**, *23*, 8200-8205.
- [42] Nosonovsky, M. *Langmuir* **2007**, *23*, 9919-9920.
- [43] Panchagnula, M. V.; Vedantam, S. *Langmuir* **2007**, *23*, 13242.
- [44] Oliver, J. F.; Huh, C.; Mason, S. G. *J. Colloid Interface Sci.* **1977**, *59*, 568-81.
- [45] Oliver, J. F.; Huh, C.; Mason, S. G. *J. Adhesion* **1977**, *8*, 223-234.

- [46] Oliver, J. F.; Mason, S. G. *J. Colloid Interface Sci.* **1977**, *60*, 480-487.
- [47] Oliver, J. F.; Huh, C.; Mason, S. G. *Colloids Surf.* **1980**, *1*, 79-104.
- [48] Bayramli, E.; Mason, S. G. *J. Colloid Interface Sci.* **1978**, *66*, 200-202.
- [49] Mori, Y. H.; Van de Ven, T. G. M.; Mason, S. G. *Colloids Surf.* **1982**, *4*, 1-15.
- [50] Dyson, D. C. *Phys. Fluids* **1988**, *31*, 229-32.
- [51] Zhang, J.; Gao, X.; Jiang, L. *Langmuir* **2007**, *23*, 3230-3235.
- [52] Berthier, J.; Loe-Mie, F.; Tran, V. M.; Schoumacker, S.; Mittler, F.; Marchand, G.; Sarrut, N. *J. Colloid Interface Sci.* **2009**, *338*, 296-303.
- [53] Kalinin, Y. V.; Berejnov, V.; Thorne, R. E. *Langmuir* **2009**, *25*, 5391-5397.
- [54] Sheng, X.; Zhang, J.; Jiang, L. *Langmuir* **2009**, *25*, 9903-9907.
- [55] Gibbs, J. W. "Scientific Papers" **1906**, 326.
- [56] Wang, J.; Chen, D. *Langmuir* **2008**, *24*, 10174-10180.
- [57] Kurogi, K.; Yan, H.; Tsuji, K. *Colloids Surf., A* **2008**, *317*, 592-597.
- [58] Ondarcuhu, T.; Piednoir, A. *Nano Lett.* **2005**, *5*, 1744-1750.
- [59] Exstrand, C. W.; Moon, S. I. *Langmuir* **2008**, *24*, 9470-9473.
- [60] Cao, L.; Hu, H.-H.; Gao, D. *Langmuir* **2007**, *23*, 4310-4314.
- [61] Liu, J.-L.; Feng, X.-Q.; Wang, G.; Yu, S.-W. *J. Phys. Condens. Matter* **2007**, *19*, 356002/1-356002/12.
- [62] Ma, Y.; Cao, X.; Feng, X.; Ma, Y.; Zou, H. *Polymer* **2007**, *48*, 7455-7460.
- [63] Tuteja, A.; Choi, W.; Ma, M.; Mabry, J. M.; Mazzella, S. A.; Rutledge, G. C.; McKinley, G. H.; Cohen, R. E. *Science* **2007**, *318*, 1618-1622.
- [64] Ahuja, A.; Taylor, J. A.; Lifton, V.; Sidorenko, A. A.; Salamon, T. R.; Lobaton, E. J.; Kolodner, P.; Krupenkin, T. N. *Langmuir* **2008**, *24*, 9-14.
- [65] Marmur, A. *Langmuir* **2008**, *24*, 7573-7579.
- [66] Tuteja, A.; Choi, W.; McKinley, G. H.; Cohen, R. E.; Rubner, M. F. *MRS Bull.* **2008**, *33*, 752-758.
- [67] Karlsson, M.; Forsberg, P.; Nikolajeff, F. *Langmuir* **2009**.

[68] Leng, B.; Shao, Z.; de With, G.; Ming, W. *Langmuir* **2009**, *25*, 2456-2460.

[69] Wang, J. D.; Liu, F. B.; Chen, H. S.; Chen, D. R. *Appl. Phys. Lett.* **2009**, *95*, 3.

[70] Youngblood, J. P.; McCarthy, T. J. *Macromolecules* **1999**, *32*, 6800-6806.

[71] Yoshimitsu, Z.; Nakajima, A.; Watanabe, T.; Hashimoto, K. *Langmuir* **2002**, *18*, 5818-5822.

[72] Dorrer, C.; Ruehe, J. *Langmuir* **2007**, *23*, 3179-3183.

[73] Extrand, C. W. *Langmuir* **2002**, *18*, 7991-7999.

[74] Extrand, C. W. *Langmuir* **2006**, *22*, 1711-1714.

[75] Decker, E. L.; Frank, B.; Suo, Y.; Garoff, S. *Colloids Surf., A* **1999**, *156*, 177-189.

[76] Meiron, T. S.; Marmur, A.; Saguy, I. S. *J. Colloid Interface Sci.* **2004**, *274*, 637-644.

[77] Li, W.; Amirfazli, A. *Adv. Colloid Interface Sci.* **2007**, *132*, 51-68.

[78] Antonini, C.; Carmona, F. J.; Pierce, E.; Marengo, M.; Amirfazli, A. *Langmuir* **2009**, *25*, 6143-6154.

[79] Bico, J.; Thiele, U.; Quere, D. *Colloids Surf., A* **2002**, *206*, 41-46.

[80] Dorrer, C.; Ruhe, J. *Langmuir* **2008**, *24*, 1959-1964.

[81] Li, W.; Amirfazli, A. *Soft Matter* **2008**, *4*, 462-466.

[82] Li, D. *Colloids Surf., A* **1996**, *116*, 1-23.

[83] Marmur, A. *J. Colloid Interface Sci.* **1997**, *186*, 462-466.

[84] Amirfazli, A.; Chatain, D.; Neumann, A. W. *Colloids Surf., A* **1998**, *142*, 183-188.

[85] Amirfazli, A.; Kwok, D. Y.; Gaydos, J.; Neumann, A. W. *J. Colloid Interface Sci.* **1998**, *205*, 1-11.

[86] Amirfazli, A.; Neumann, A. W. *Adv. Colloid Interface Sci.* **2004**, *110*, 121-141.

[87] Lin, F. Y. H.; Li, D.; Neumann, A. W. *J. Colloid Interface Sci.* **1993**, *159*, 86-95.

Annex A Supplemental Information for Chapter 1

S1. Feature Size measurement

Feature sizes were measured by Scanning Electron Microscope (SEM) and White Light Confocal Microscopy (LCM) for the microgeometries of Tables 1, 2 and 3. Note that there are two cases in experimental process for each needed size, i.e., one is set to be a value the same to the ideal size and the other is set to be a value about 7% larger than the ideal size during L-edit design. The results show that the latter one with sizes 7% larger can finally get results approximate to the ideal sizes we need after lithography and reactive ion etching. Detail information is given in Table A1-7 to A1-15.

Table A1-7. L-Edit settings and experimental results for square post arrays of microgeometrical parameters corresponding to Table 1 (S=256, $f_a=0.28$)

Square	$a / \mu\text{m}$	$\lambda(a+b) / \mu\text{m}$
Ideal Sizes	16	30
Case 1	17	30
SEM	16.08 ± 0.09	29.94
LCM	16.46 ± 0.14	30.01 ± 0.09
Case 2	16	30
SEM	15.12 ± 0.17	29.64
LCM	15.11 ± 0.05	30.03 ± 0.10

Table A1-8. L-Edit settings and experimental results for triangle post arrays of microgeometrical parameters corresponding to Table 1 (S=256, $f_a=0.28$)

Triangle	$a / \mu\text{m}$	$\lambda(a+b) / \mu\text{m}$
Ideal Sizes	24.3	30
Case 3	26	30
SEM	24.66 ± 0.12	28.24
LCM	24.49 ± 0.10	30.03 ± 0.16
Case 4	24.3	30
SEM	22.91 ± 0.10	30
LCM	23.02 ± 0.14	29.97 ± 0.05

Table A1-9. L-Edit settings and experimental results for circle post arrays of microgeometrical parameters corresponding to Table 1 (S=256, $f_a=0.28$)

Circle	$a / \mu\text{m}$	$\lambda(a+b) / \mu\text{m}$
Ideal Sizes	18	30
Case 5	19.2	30
SEM	18.16	29.23
LCM	18.51 ± 0.15	30.04 ± 0.12
Case 6	18	30
SEM	17.20 ± 0.10	28.79
LCM	17.79 ± 0.06	30.03 ± 0.09

Table A1-10. L-Edit settings and experimental results for square post arrays of microgeometrical parameters corresponding to Table 2 (S=64, $f_a=0.28$)

Square	$a / \mu\text{m}$	$\lambda(a+b) / \mu\text{m}$
Ideal Sizes	8	15
Case 7	8.5	15
SEM	7.71 ± 0.03	14.22
LCM	7.9 ± 0.13	15.06
Case 8	8	15
SEM	7.54 ± 0.22	14.24
LCM	7.94 ± 0.06	15.06 ± 0.13

Table A1-11. L-Edit settings and experimental results for triangle post arrays of microgeometrical parameters corresponding to Table 2 (S=64, $f_a=0.28$)

Triangle	$a / \mu\text{m}$	$\lambda(a+b) / \mu\text{m}$
Ideal Sizes	12.2	15
Case 9	13	15
SEM	12.04 ± 0.02	14.32
LCM	11.98 ± 0.05	15.12 ± 0.10
Case 10	12.2	15
SEM	10.62 ± 0.06	13.97
LCM	10.41 ± 0.05	15.03 ± 0.05

Table A1-12. L-Edit settings and experimental results for circle post arrays of microgeometrical parameters corresponding to Table 2 (S=64, $f_a = 0.28$)

Circle	$a / \mu\text{m}$	$\lambda(a+b) / \mu\text{m}$
Ideal Sizes	9	15
Case 11	9.6	15
SEM	8.56 \pm 0.08	14.34
LCM	8.66 \pm 0.14	15 \pm 0.05
Case 12	9	15
SEM	7.97 \pm 0.14	14.25
LCM	7.99 \pm 0.09	15 \pm 0.05

Table A1-13. L-Edit settings and experimental results for square post arrays of microgeometrical parameters corresponding to Table 3 (S=64, $f_a = 0.071$)

Square	$a / \mu\text{m}$	$\lambda(a+b) / \mu\text{m}$
Ideal Sizes	8	30
Case 16	8	30
SEM	6.97 \pm 0.17	28.21
LCM	6.85 \pm 0.06	30.07 \pm 0.07
Case 13	8.5	30
SEM	7.62 \pm 0.25	28.4
LCM	7.62 \pm 0.09	30.09 \pm 0.05

Table A1-14. L-Edit settings and experimental results for triangle post arrays of microgeometrical parameters corresponding to Table 3 (S=64, $f_a = 0.071$)

Triangle	$a / \mu\text{m}$	$\lambda(a+b) / \mu\text{m}$
Ideal Sizes	12.2	30
Case 17	12.2	30
SEM	10.47 \pm 0.06	28.45
LCM	10.19	30.21
Case 14	13	30
SEM	12.02 \pm 0.11	29.36
LCM	11.77 \pm 0.21	29.86 \pm 0.07

Table A1-15. L-Edit settings and experimental results for circle post arrays of microgeometrical parameters corresponding to Table 3 (S=64, $f_a = 0.071$)

Circle	$a / \mu\text{m}$	$\lambda (=a+b) / \mu\text{m}$
Ideal Sizes	9	30
Case 18	9	30
SEM	8.06±0.12	28.25
LCM	7.76±0.07	29.94±0.13
Case 15	9.6	30
SEM	8.94±0.22	29.32
LCM	8.2±0.06	30.09±0.10

S2. CA data for Figure 1-11a and b

Table A2-16. Variations of advancing (θ_a), receding (θ_r) CAs and contact angle hysteresis (CAH) with respect to pattern types and geometrical parameters corresponding to Tables 1 (T1: $f_a = 0.28$, $S=256\mu\text{m}^2$), 2 (T2: $f_a = 0.28$, $S=64\mu\text{m}^2$) and 3 (T3: $f_a=0.071$, $S=64\mu\text{m}^2$) for post height 20 μm . SD represents the standard deviation for measurements.

	$\theta_a(^{\circ})$	SD- θ_a	$\theta_r(^{\circ})$	SD- θ_r	CAH($^{\circ}$)	SD-CAH	$f_{\text{real}} \text{ from } \theta_r$	$\theta_{s,adv}(^{\circ})$
T1-Square	171.9	1.19	127.6	1.79	44.2	2.15	0.47	168.1
T1-Triangle	174.3	1.08	131.6	3.81	42.7	3.96	0.40	171.0
T1-Circle	172.9	1.62	130.6	1.95	42.3	2.53	0.42	169.0
T2-Square	170.1	1.06	136.0	1.74	34.1	2.04	0.34	162.8
T2-Triangle	170.6	3.01	136.4	2.89	34.2	4.17	0.33	163.6
T2-Circle	171.3	3.16	135.4	2.87	35.9	4.27	0.35	165.1
T3-Square	174.3	1.1	147.0	2.61	27.3	3.38	0.19	167.0
T3-Triangle	172.6	2.43	144.4	1.2	28.2	2.71	0.22	164.3
T3-Circle	173.8	2.19	142.9	3.06	30.9	3.76	0.24	167.5

Table A2-17. Variations of advancing (θ_a), receding (θ_r) CAs and contact angle hysteresis (CAH) with respect to pattern types and geometrical parameters corresponding to Tables 1 (T1: $f_a = 0.28$, $S = 256\mu\text{m}^2$), 2 (T2: $f_a = 0.28$, $S = 64\mu\text{m}^2$) and 3 (T3: $f_a = 0.071$, $S = 64\mu\text{m}^2$) for post height 30 μm . SD represents the standard deviation for measurements.

	$\theta_a(^{\circ})$	SD- θ_a	$\theta_r(^{\circ})$	SD- θ_r	CAH($^{\circ}$)	SD-CAH	freal from θ_r	$\theta_{s,adv}(^{\circ})$
T1-Square	173.4	1.19	128.1	2.63	45.3	2.89	0.46	170.3
T1-Triangle	172.1	0.72	130.9	1.1	41.2	1.32	0.42	167.7
T1-Circle	169.8	1.83	129.0	0.86	40.9	2.47	0.45	164.7
T2-Square	170.3	1.23	135.2	1.12	35.1	1.67	0.35	163.5
T2-Triangle	166.8	0.93	133.0	2.15	33.8	2.34	0.38	158.6
T2-Circle	169.4	1.58	135.6	1.6	33.9	2.25	0.34	161.9
T3-Square	174.0	1.61	148.0	2.84	26.1	3.26	0.18	166.0
T3-Triangle	170.3	2.55	145.2	1.2	25.1	2.81	0.21	159.0
T3-Circle	172.3	1.25	148.0	2.97	24.3	3.22	0.18	161.9

This page intentionally left blank.

List of symbols/abbreviations/acronyms/initialisms

CA	Contact Angle
CAH	Contact Angle Hysteresis
DND	Department of National Defence
DRDC	Defence Research & Development Canada
DRDKIM	Director Research and Development Knowledge and Information Management
DCL	Drop contact line
f_l	fraction of the solid-liquid interface
f_2	fraction of the liquid-air interface
f_a	Solid-liquid contact area fraction
f_l ,	Local contact fraction is treated as a local linear fraction of the contact line
f_{real}	Real local solid-liquid contact fraction in the region of DCL
γ_{la}	Interfacial tension at liquid-air interface
γ_{sa}	Interfacial tension at solid-air interface
γ_{ls}	Interfacial tension at liquid-solid interface
LCM	White Light Confocal Microscopy (LCM)
r	Roughness
R&D	Research & Development
SEM	Scanning Electron Microscope
SHS	Superhydrophobic surfaces
θ_r and θ_a	Apparent receding and advancing CAs
$\theta_{s,rec}$ and $\theta_{s,adv}$	Local receding and advancing CAs at the solid-liquid contact part
θ_Y	Young Contact Angle
θ_W	Wenzel Contact Angle

This page intentionally left blank.

Distribution list

Document No.: DRDC Atlantic CR 2010-329

LIST PART 1: Internal Distribution by Centre

- 3 DRDC Atlantic Library
- 1 Paul Saville, DRDC Atlantic
- 1 Calvin Hyatt, DRDC Atlantic

5 TOTAL LIST PART 1

LIST PART 2: External Distribution by DRDKIM

- 1 Library and Archives Canada, Attn: Military Archivist, Government Records Branch
- 1 DRDKIM
- 1 Scott Duncan, DRDC Suffield
- 1 Dr Amirfazli, Department Mechanical Engineering, University of Alberta, Edmonton, Alberta, T6G 2G8

4 TOTAL LIST PART 2

9 TOTAL COPIES REQUIRED

This page intentionally left blank.

DOCUMENT CONTROL DATA

(Security classification of title, body of abstract and indexing annotation must be entered when the overall document is classified)

<p>1. ORIGINATOR (The name and address of the organization preparing the document. Organizations for whom the document was prepared, e.g. Centre sponsoring a contractor's report, or tasking agency, are entered in section 8.)</p> <p>Alidad Amirfazli Department of Mechanical Engineering University of Alberta Edmonton, Alberta T6G 2G8</p>		<p>2. SECURITY CLASSIFICATION (Overall security classification of the document including special warning terms if applicable.)</p> <p align="center">UNCLASSIFIED</p>	
<p>3. TITLE (The complete document title as indicated on the title page. Its classification should be indicated by the appropriate abbreviation (S, C or U) in parentheses after the title.)</p> <p align="center">Superomniphobic Surfaces for Military Applications: Nano- and Micro-Fabrication Methods: Chapter 1: Lithographic Fabrication of Surfaces with Different Microgeometries and Investigation of Their Wetting Behaviour</p>			
<p>4. AUTHORS (last name, followed by initials – ranks, titles, etc. not to be used)</p> <p align="center">Amirfazli, Alidad</p>			
<p>5. DATE OF PUBLICATION (Month and year of publication of document.)</p> <p align="center">January 2011</p>	<p>6a. NO. OF PAGES (Total containing information, including Annexes, Appendices, etc.)</p> <p align="center">60</p>	<p>6b. NO. OF REFS (Total cited in document.)</p> <p align="center">87</p>	
<p>7. DESCRIPTIVE NOTES (The category of the document, e.g. technical report, technical note or memorandum. If appropriate, enter the type of report, e.g. interim, progress, summary, annual or final. Give the inclusive dates when a specific reporting period is covered.)</p> <p align="center">Contract Report</p>			
<p>8. SPONSORING ACTIVITY (The name of the department project office or laboratory sponsoring the research and development – include address.)</p> <p align="center">Defence R&D Canada – Atlantic 9 Grove Street P.O. Box 1012 Dartmouth, Nova Scotia B2Y 3Z7</p>			
<p>9a. PROJECT OR GRANT NO. (If appropriate, the applicable research and development project or grant number under which the document was written. Please specify whether project or grant.)</p> <p align="center">12SZ20</p>	<p>9b. CONTRACT NO. (If appropriate, the applicable number under which the document was written.)</p> <p align="center">W7707-098197</p>		
<p>10a. ORIGINATOR'S DOCUMENT NUMBER (The official document number by which the document is identified by the originating activity. This number must be unique to this document.)</p>	<p>10b. OTHER DOCUMENT NO(s). (Any other numbers which may be assigned this document either by the originator or by the sponsor.)</p> <p align="center">DRDC Atlantic CR 2010-329</p>		
<p>11. DOCUMENT AVAILABILITY (Any limitations on further dissemination of the document, other than those imposed by security classification.)</p> <p align="center">Unlimited</p>			
<p>12. DOCUMENT ANNOUNCEMENT (Any limitation to the bibliographic announcement of this document. This will normally correspond to the Document Availability (11). However, where further distribution (beyond the audience specified in (11) is possible, a wider announcement audience may be selected.)</p> <p align="center">Unlimited</p>			

13. ABSTRACT (A brief and factual summary of the document. It may also appear elsewhere in the body of the document itself. It is highly desirable that the abstract of classified documents be unclassified. Each paragraph of the abstract shall begin with an indication of the security classification of the information in the paragraph (unless the document itself is unclassified) represented as (S), (C), (R), or (U). It is not necessary to include here abstracts in both official languages unless the text is bilingual.)

Recent rapid improvements of micro/nanofabrication techniques have allowed us to prepare patterned surfaces with controlled topographic structures. In this report, three kinds of patterned surfaces, i.e., square, triangle and circle post array surfaces, have been prepared on silicon wafers. On such surfaces, for the same roughness or solid-liquid contact fraction value, different surface textures can exhibit completely different wetting behaviour. Effects of various microgeometrical parameters, such as length scale effect, edge/corner pinning effect, geometrical shape effect, direction-dependent effect, etc., on wetting have been investigated. For the patterned surfaces with fixed solid area fraction, a smaller microgeometrical length scale can induce a smaller advancing contact angle and a larger receding contact angle, when it is compared to a larger microgeometrical length scale. Competing factors such as solid area fraction and solid linear fraction are found to be responsible for such effect. Moreover, it is also revealed that there is a strong dependence of directions for surface wettability on the patterned surfaces. Different edge/corner pinning effects, including the pinning length and pinning point density, in various directions are suggested to be taken into consideration for affecting the surface wetting behaviour.

Les progrès rapides qu'ont connus récemment les techniques de microfabrication et de nanofabrication nous ont permis de préparer des surfaces à motif qui possèdent des structures topographiques contrôlées. Dans le cadre des travaux qui font l'objet du présent rapport, trois types de surfaces à motif ont été préparées sur des plaquettes de silicium, soit des surfaces post-matrice à carrés, à triangles et à cercles. Pour des surfaces de cette nature qui présentent une rugosité identique et une valeur égale de la fraction de contact solide-liquide, les diverses textures superficielles des surfaces peuvent avoir un comportement au mouillage totalement différent. On a étudié les effets de divers paramètres microgéométriques sur le mouillage, notamment l'effet d'échelle de longueur, l'effet d'ancrage des bords et des coins, l'effet de la forme géométrique et l'effet qui dépend de l'orientation. Dans le cas des surfaces à motif qui présentent une fraction superficielle solide fixe, une faible échelle de longueur microgéométrique peut se traduire par un angle de contact à l'avancement plus petit et un angle de contact au retrait plus important, comparativement à une échelle plus large. Les résultats indiquent qu'un effet de cette nature est attribuable à des facteurs concurrentiels tels que la fraction superficielle solide et la fraction linéaire solide. De plus, ils révèlent que la mouillabilité superficielle des surfaces à motif dépend grandement des orientations des caractéristiques. Les données laissent supposer qu'il faut tenir compte de différents effets d'ancrage des bords et des coins, y compris la longueur d'ancrage et la densité des points d'ancrage, dans le cas de diverses orientations, car ils pourraient influer le comportement au mouillage de la surface.

14. KEYWORDS, DESCRIPTORS or IDENTIFIERS (Technically meaningful terms or short phrases that characterize a document and could be helpful in cataloguing the document. They should be selected so that no security classification is required. Identifiers, such as equipment model designation, trade name, military project code name, geographic location may also be included. If possible keywords should be selected from a published thesaurus, e.g. Thesaurus of Engineering and Scientific Terms (TEST) and that thesaurus identified. If it is not possible to select indexing terms which are Unclassified, the classification of each should be indicated as with the title.)

Contact Angle; Superhydrophobic; Superoleophobic; Superomniphobic; Wettability

This page intentionally left blank.

Defence R&D Canada

Canada's leader in defence
and National Security
Science and Technology

R & D pour la défense Canada

Chef de file au Canada en matière
de science et de technologie pour
la défense et la sécurité nationale



www.drdc-rddc.gc.ca